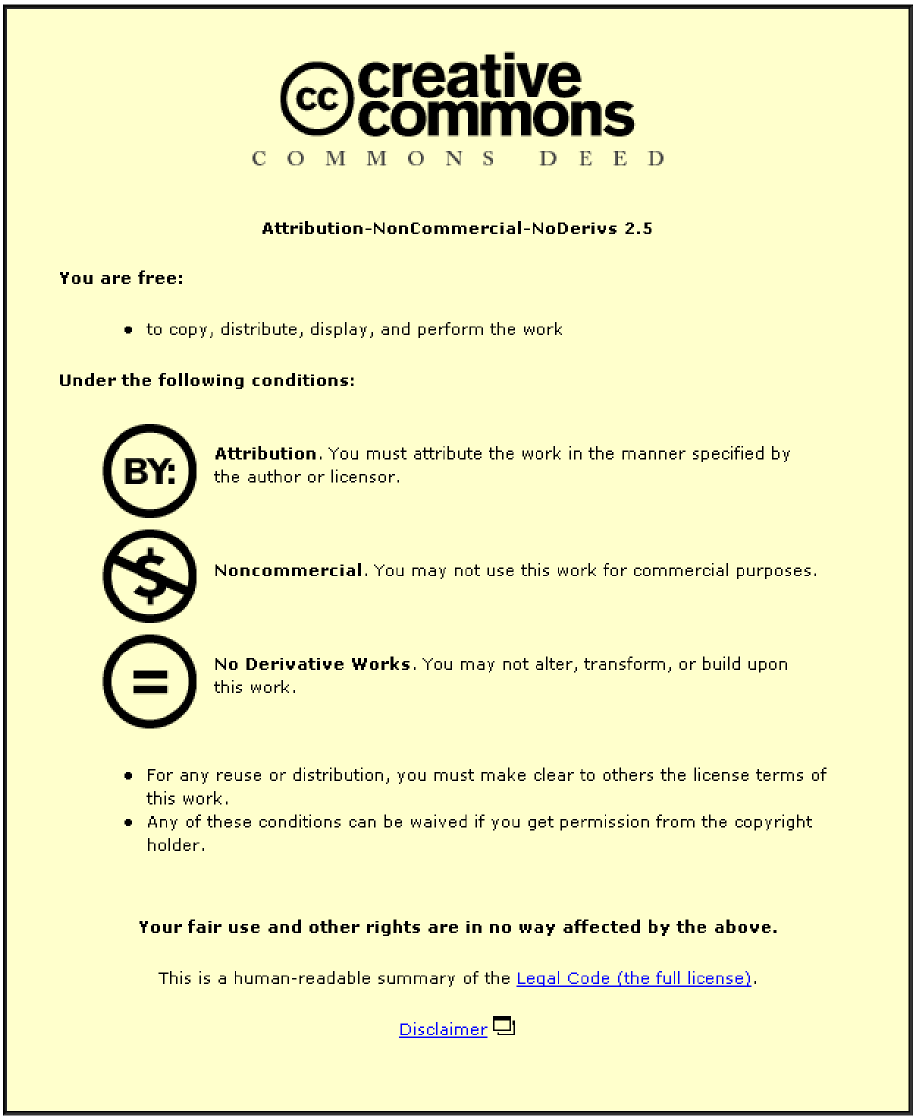

JOURNAL OF GEOPHYSICAL RESEARCH, VOL. 109, B10102, doi:10.1029/2004JB003041, 2004

"Plate-like" subsidence of the East Pacific Rise–South Pacific superswell system

J. K. Hillier and A. B. Watts
Department of Earth Sciences, University of Oxford, Oxford, UK

Received 24 February 2004; revised 21 June 2004; accepted 21 July 2004; published 21 October 2004.

[1] In previous studies the removal of small-scale features such as seamounts and oceanic islands from bathymetry has revealed a large and unusually shallow region in the South Pacific Ocean, which, at 3000 km wide and up to 1 km high, has been dubbed a "superswell." These studies use statistical techniques based on finding the modal depth of the bathymetry. Such an analysis, however, does not completely isolate these features, or their associated oceanic plateaus and localized hot spot swells, from the ridge-generated regional bathymetry upon which they are superimposed. Accordingly, a technique is required that passes beneath topographic constructs rather than through them, as is the tendency of the mean, median, or mode. We have developed an algorithm, MiMIC, that reproducibly removes all these features and reveals the large-scale bathymetric trends in a manner based upon and consistent with manual interpretation. Application of the algorithm to bathymetry data in the southwest Pacific shows that the depth anomaly with respect to a cooling plate model changes steadily from being too deep at the East Pacific Rise (EPR) crest to being too shallow at the superswell. The largest shallow anomaly of 712 ± 66 m occurs at 98 Ma, not 1300 m at 65 Ma, as has been previously suggested. Most significantly, the superswell appears to be part of a large-scale, "plate-like," subsidence that extends to the EPR crest, rather than an isolated shallowing that reverses the subsidence and causes uplift. We interpret the plate-like subsidence as due in part to cooling of the oceanic lithosphere and in part to a lateral temperature gradient in the underlying asthenosphere which is maintained by the flow of relatively hot material from beneath the superswell toward the relative cold material beneath the EPR. The best fit model implies a lateral temperature gradient of 0.014°C km^{-1} and is in general accord with the available effective elastic thickness, crustal thickness, heat flow, and seismic tomography data. *INDEX TERMS:* 8120 Tectonophysics: Dynamics of lithosphere and mantle—general; 8194 Tectonophysics: Instruments and techniques; 9355 Information Related to Geographic Region: Pacific Ocean; 3094 Marine Geology and Geophysics: Instruments and techniques; *KEYWORDS:* superswell, Pacific, bathymetry

Citation: Hillier, J. K., and A. B. Watts (2004), ''Plate-like'' subsidence of the East Pacific Rise–South Pacific superswell system, *J. Geophys. Res.*, *109*, B10102, doi:10.1029/2004JB003041.

1. Introduction

[2] The cooling plate model successfully describes the general form of the subsidence of oceanic crust away from a mid-ocean ridge crest. A 125 ± 10 km thick cooling plate with a basal temperature of 1350° ± 275°C, for example, explains well depth-age data from the North Atlantic and North Pacific Oceans [*Parsons and Sclater*, 1977], and this model provides a standard against which depth anomalies [*Menard*, 1973] may be defined.

[3] One of the world's largest depth anomalies is in the South Pacific Ocean (Figure 1). Dubbed a "superswell" by *McNutt and Fischer* [1987], the depth anomaly reportedly has a maximum amplitude of $\geq$1 km [*McNutt and Sichoix*, 1996; *Sichoix et al.*, 1998], a width of approximately 3000 km [*McNutt*, 1998], and covers some 15 million km^2 of the seafloor [*McNutt and Fischer*, 1987].

[4] The superswell region (160°–130°W, 3°–33°S) [*McNutt and Fischer*, 1987], however, is characterised by intense multiscale volcanism. At a "small" scale there are a number of islands, seamounts are more abundant [*Bemis and Smith*, 1993] than on normal Pacific oceanic lithosphere [*Smith and Jordan*, 1988], and there are aseismic ridges [*Winterer and Sandwell*, 1987; *Goodwillie*, 1995]. At a "medium" scale there is at least one oceanic plateau (e.g., Tuamotu [e.g., *Talandier and Okal*, 1987]) and a cluster [*McNutt and Judge*, 1990] of isolated [*Sichoix et al.*, 1998] hot spot swells (e.g., Society, Marquesas and Austral). These topographic features do not contribute to the superswell [*McNutt and Fischer*, 1987; *McNutt*, 1998; *Sichoix et al.*, 1998] and hinder its isolation because they make it difficult to determine a "regional" depth, which represents the upper surface of the superswell, from the bathymetry.

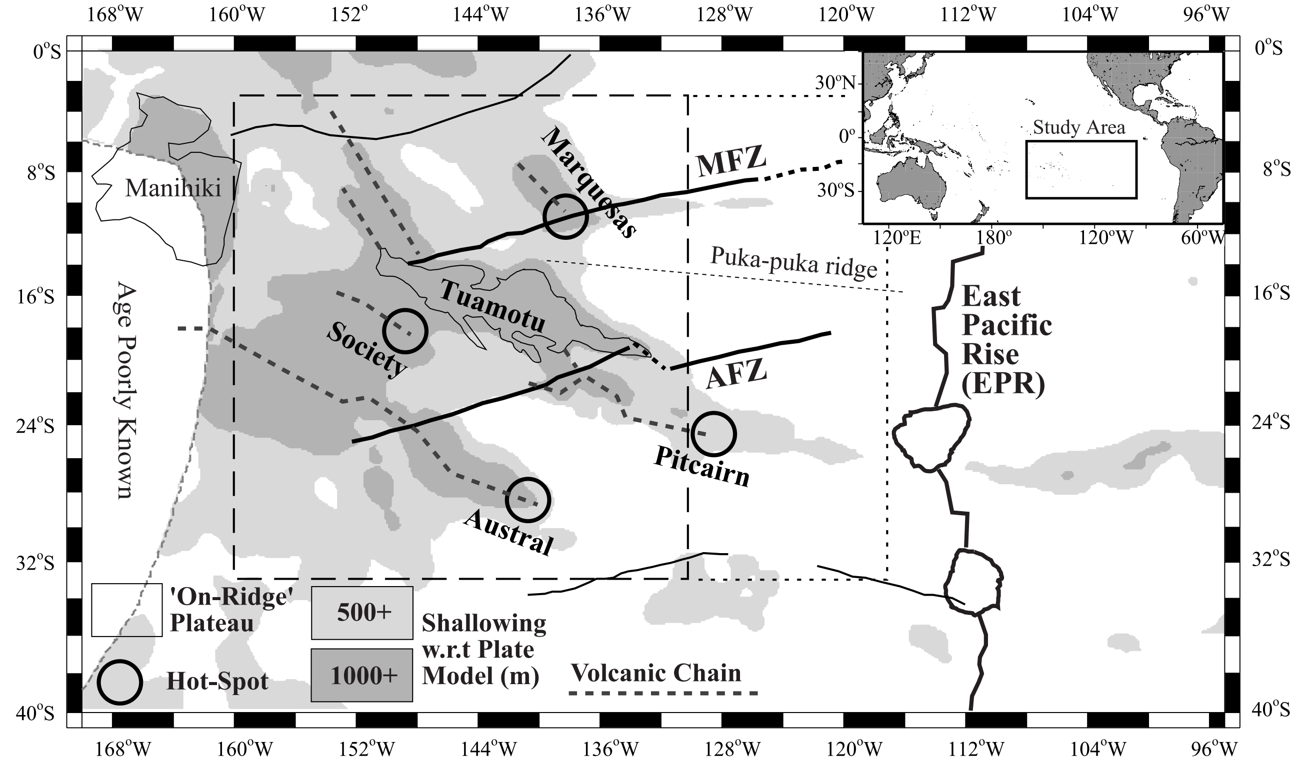

Figure 1. Map of deviations from an expected depth, or depth anomalies [*Menard*, 1973], in the South Pacific region. As *McNutt and Fischer* [1987], expectations of depth come from predictions of the cooling plate model of *Parsons and Sclater* [1977]. Light grey shades are positive (shallow) anomalies of ≥500 m, and dark shades are anomalies of ≥1 km. The long-dashed box is the region studied by *McNutt and Fischer* [1987]. The short-dashed box extends their area and indicates the additional area studied in this paper. MFZ, Marquesas Fracture Zone; AFZ, Austral Fracture Zone; dashed grey lines are volcanic chains. Circles indicate clusters of recent volcanism [*Clouard and Bonneville*, 2001] or "hot spots" [e.g., *Fowler*, 1990], which, except possibly Pitcairn [*Binard et al.*, 1992], are associated with bathymetric swells [*McNutt and Fischer*, 1987; *Sichoix et al.*, 1998; *McNutt and Bonneville*, 2000], commonly called hot spot swells.

[5] *McNutt and Fischer* [1987] suggested a method for overcoming this difficulty. They used 5′ SYNBAPS [*Van Wykhouse*, 1973] (or DBDB-5) bathymetry data and the *Parsons and Sclater* [1977] cooling plate model, together with a contoured density plot of depth-age pairs [*Renkin and Sclater*, 1988], to show that 20 Ma old seafloor (125°W) is 250 m shallower than expected, and that the superswell anomaly increases to 750 m for 80 Ma seafloor (160°W).

[6] Density contour plots emphasize the mode, or most frequent value, and mostly mask the bias to shallow depths present in simple depth averages (e.g., mean and median). For example, the Tuamotu plateau which is prominent as a rise in the light grey low-density contour (Figure 2) is much reduced in the dark grey high-density contour. This is because the high-density contour reflects the regional seafloor depths better than that of the low-density contour. This assertion, however, is based upon an assumption, which applies to all modal techniques, that the regional bathymetry is always sufficiently flat to dictate the mode, even when only small areas of "normal" regional seafloor are present [*Levitt and Sandwell*, 1996].

[7] *Levitt and Sandwell* [1996] used ETOPO-5 (which incorporates SYNBAPS) bathymetry data between the EPR (115°W) and the Tuamotu Plateau (135°W) and showed that 28 to 37 Ma old oceanic crust is concentrated at depths of about 4000 m, which is shallower than inferred from shipboard data. The tendency for ETOPO-5 [*National Oceanic and Atmospheric Administration* (*NOAA*), 1988] to show such flatness, particularly at multiples of 500 m, has been noted by *Smith* [1993]. *Levitt and Sandwell* [1996] therefore argued that the depth anomaly of 28 to 37 Ma oceanic crust results from the "splining of sparse seamount-derived contour maps, which are unrepresentative of the ambient seafloor depth"; this was later labelled the "bad data" hypothesis to explain the superswell phenomenon by *McNutt* [1998].

[8] To establish what they called the "correct" seafloor depth between the EPR and the Tuamotu Plateau, *Levitt and Sandwell* [1996] used swath bathymetry data and an automated mode estimation technique. They claim that the estimated mode (which is demonstrably more "robust" [*Box*, 1953] than other filters and is therefore less affected by constructional volcanic features than the mean or median) provides more accurate (i.e., deeper) estimates of unperturbed seafloor depths, even for a data set acquired along an individual ridge such as Puka-Puka. The resultant modal depth anomaly over 15–35 Ma old (135°W–123°W) sea-

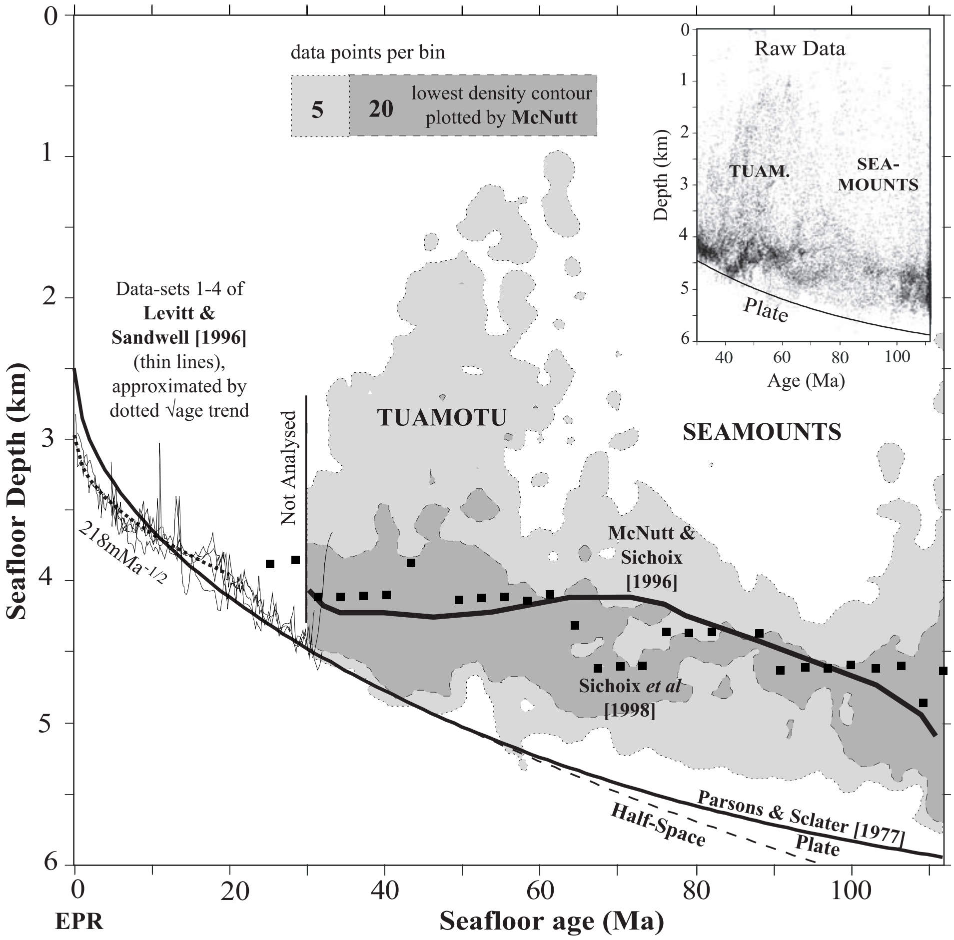

Figure 2. Density contour plot of depth and age data in the superswell region. Grey shades show the relationship between depth and age in bins of 2 Ma × 100 m, as were used by *McNutt and Sichoix* [1996]. Light shading indicates infrequently occurring ($\geq$5 per bin) depths. Dark shading indicates commonly occurring ($\geq$20 per bin) depths. The density contour plots reveal a superswell about 1 km shallower than the plate model of *Parsons and Sclater* [1977]. The heavy solid line indicates our estimate of the strongest modes in the data of *McNutt and Sichoix* [1996], the maximum shallowing of which is $\sim$1300 m. Filled squares indicate the strongest modes in the data of *Sichoix et al.* [1998]. Thin lines show the modal depths of young (i.e., <40 Ma) seafloor from Figures 5a–5d of *Levitt and Sandwell* [1996]. The inset shows 0.1° × 0.1° modes of raw depth soundings. EPR, East Pacific Rise.

floor is small (<200 m), and decreases to almost zero for the oldest of these ages. They therefore suggested that seafloor east of the Tuamotu Plateau is of normal depth for its age, thereby casting doubt on the existence of a superswell.

[9] *McNutt and Sichoix* [1996] question, however, how representative an analysis is that is based on 5 ship tracks and only overlaps the eastern extremity of the superswell (137°W–130°W). They therefore used a more extensive data set of original, quality controlled, single beam, bathymetry data. The data include the depths of 30–110 Ma (160°W–130°W) seafloor, and being raw "point" data cannot contain errors propagated from contouring. To give the data an even spatial weighting, which eliminates a bias toward heavy data concentrations (e.g., near ports), a 0.1° × 0.1° spatial mode was used. The preprocessed data was then displayed as density contours, in a similar way to *McNutt and Fischer* [1987]. *McNutt and Sichoix* [1996] reassert that 30–35 Ma seafloor is typically 250 m shallower than expected, the depth anomaly increases to $\geq$1300 m on older seafloor (Figure 2), and that the superswell does indeed exist.

[10] *Sichoix et al.* [1998] subsequently refined the density contouring technique by manually limiting the areas of seafloor that were included. They found a 1000 m superswell depth anomaly that increased between 40–80 Ma and then decreased (Figure 2). However, there is still a concern as to whether "representative" [*Levitt and Sandwell*, 1996] or "typical" [*Sichoix et al.*, 1998] seafloor depths estimated by the mode actually represent regional depth.

[11] In French Polynesia, areas where the regional depth can be measured directly are rare. Thus it may be inappropriate to use common depth, modal averaging techniques to estimate regional depth. With increasingly intense volcanism, the mode detects the decreasing signal with increasing unreliability and becomes "in some senses noisy" [*Smith*, 1990]. Low-pass filters can suppress this "chattering" [*Yanada and Ohnishi*, 1999; *Bartoszewicz*, 2000; *Xia et al.*, 2000], but only within limits. This is illustrated if the

seafloor approaches an idealized sawtooth morphology. Then, all depths become almost equally likely, the mode is highly erratic, and smoothing of the scattered estimates is expected to approximate the mean height of the topography. What is required is a filter that passes beneath bathymetric features rather than through them. This is the case, at least, for volcanism that is superimposed on the superswell.

[12] The separation of small-scale features such as oceanic islands and seamounts from bathymetry data is an important geodynamic objective which has implications for the origin of the superswell. *McNutt and Fischer* [1987] suggested that the superswell was caused by regional thermal rejuvenation of the lithosphere. They cited the low elastic thickness of the lithosphere, T_e, estimated by *Calmant* [1987] and *Calmant and Cazenave* [1987] as evidence for elevated temperatures in the region. However, *Stein and Abbott* [1991] found no evidence that the surface heat flow over the superswell is any higher than would be expected for the age of the underlying oceanic crust. Furthermore, T_e is normal for the plate and load ages [*Filmer et al.*, 1993; *Goodwillie and Watts*, 1993; *McNutt et al.*, 1997; *McNutt*, 1998]. *Sichoix et al.* [1998] reconsidered the role of the lithosphere in models for the origin of the superswell. They favored a model in which the superswell was maintained by some form of dynamic motion in the underlying convecting mantle.

[13] The purpose of this paper is to reevaluate the relationship between bathymetry and crustal age in the superswell region and consequently the mechanisms that are responsible for it. In particular, we develop an algorithm, MiMIC, that entirely removes bathymetric features, whatever their scale or spatial density. Application of MiMIC to bathymetric data reveals that the superswell is part of a plate-like subsidence which extends to the EPR, rather than an isolated region of unusually shallow seafloor. We discuss the origins of a coupled superswell-EPR system and its implications for oceanic plate structure and mantle dynamics.

2. Multiscale Nature of Bathymetry

[14] The seafloor comprises a multiscale hierarchy of bathymetric features. In order to isolate poorly defined large-scale features such as the superswell, a technique is required that accurately removes all those smaller-scale features such as small-scale seamounts and oceanic islands, and medium-scale oceanic plateaus and localized hot spot swells.

[15] The problem is illustrated in Figure 3 which shows a bathymetry profile of the South Pacific from the Tuamotu Plateau, across the Society islands, to a group of seamounts referred to as the Savannah seamounts [*Bonneville et al.*, 1997; *Sichoix et al.*, 1998]. The profile shows a number of bathymetric features (light grey shade in Figure 3) that range in height from a few hundreds of meters to a few km and in width from few tens to a few hundred km. The features rise above a bathymetry that includes medium-scale trends such as hot spot swells, in this case Society [*Crough*, 1978; *Binard et al.*, 1991; *Sichoix et al.*, 1998]. The hot spot swell (dark grey shade in Figure 3) is, in turn, superimposed on the larger-scale depth that increases with age. In each case, the context-dependent term "regional" refers to the larger scale of the two trends [e.g., *Wessel*, 1998].

[16] The bold lines on the expanded profile in Figure 3 show attempts using median, mode and mean sliding window spatial filters to separate the small-scale bathymetric features along the profile from the regional seafloor depth upon which they are superimposed. The mean clearly is inadequate. This filter passes through or above these features rather than underneath them, thereby underestimating their true dimensions. The median and mode perform satisfactorily when their widths are optimized to operate on individual features [see also *Wessel*, 1998], as they have been for the two largest features in Figure 3. However, both these filters operate on a fixed window width and fail when the objective is to accurately remove all of the variably sized small-scale features from a single bathymetric profile.

[17] Some of the small-scale features in Figure 3 might be removed using an array of optimal filters such as used in "parallel" [*Yatawara et al.*, 1991] or "multichannel" [*Lin and Hsueh*, 2000] data processing schemes. However, automating the selection of the appropriate filter presents its own difficulties, and while progress has been made in the case of a single bathymetric feature [*Wessel*, 1998], a procedure has yet to be devised for the multiscale problem.

[18] Another approach might be to develop a filtering scheme that ignores scale entirely. For example, seamounts, whatever their size, may be approximated as flat-topped cones or frustums [*Jordan et al.*, 1983; *Smith and Jordan*, 1988; *Smith*, 1988] whose sides slope more steeply than their surroundings. However, a frustum is only an approximation. Seamounts collectively span a wide range [*Smith*, 1996] of possible frustum parameters [*Jordan et al.*, 1983], and thus there is no simple description of their shape. Furthermore, their sides slope steeply at a wide range of spatial scales, and so it is necessary to smooth (e.g., sliding arithmetic mean) gradients at the scale of a feature. Despite these difficulties, we do recognize small-scale features on the seafloor such as seamounts [e.g., *Jordan et al.*, 1983; *Smith and Jordan*, 1988; *Smith*, 1988] and can manually, at least, pick the regional seafloor depth even in their presence [e.g., *Menard*, 1973; *Sclater et al.*, 1975; *Parsons and Sclater*, 1977].

3. MiMIC: An Algorithm for the Separation of Small-Scale From Large-Scale Bathymetry

[19] We have developed a technique, the Micro Macro Interpretation Construct, or MiMIC, which simulates manual interpretation of asymmetric multiscale bathymetry data. It is a nonlearning, or expert algorithm which operates according to explicitly stated rules. This is in contrast to learning algorithms, commonly called neural networks. We describe here, and in further detail in Appendix A, the operation of MiMIC.

[20] In manual interpretation a seamount, for example, may be identified directly and a regional seafloor depth passing beneath it then deduced. This is effective even where areas of normal depth seafloor are rare. Underlining bathymetric features along a profile, say from left to right, thus requires that the data ahead be considered as "highs" (i.e., relatively shallow regions). Highs of a characteristic shape (e.g., a seamount) may then be identified as bathy-

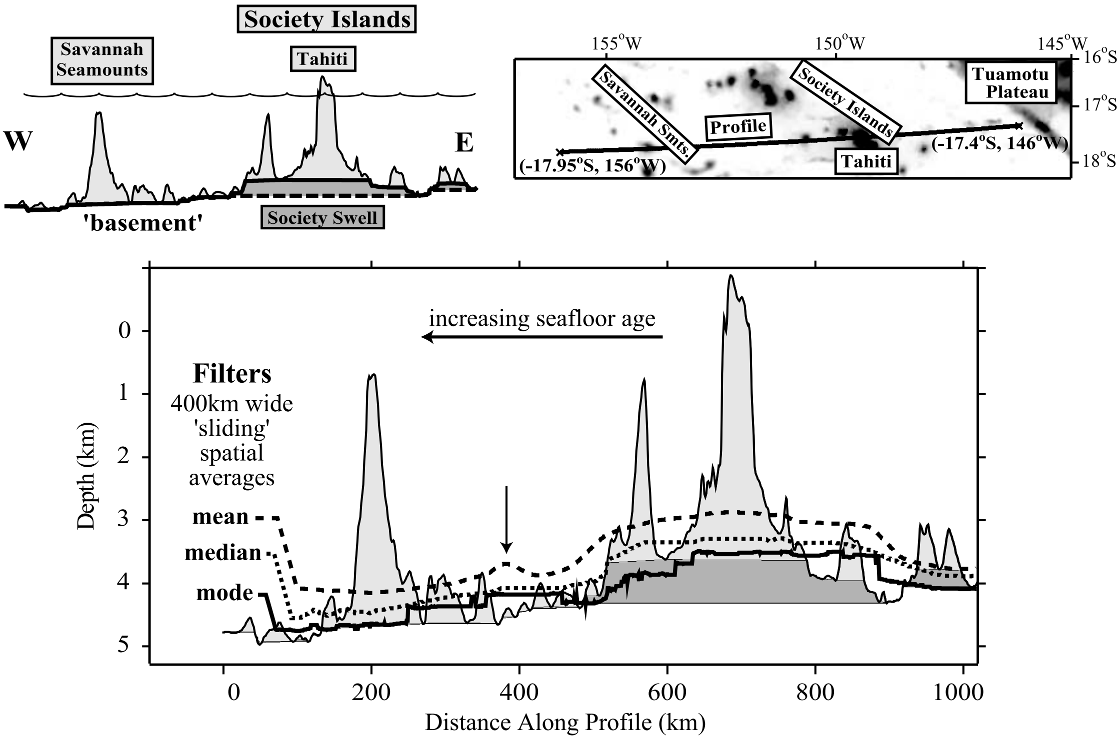

Figure 3. Comparison of the mean, median, and mode sliding window filters of the bathymetry along a profile that extends (top right) from the Tuamotu Plateau, across the Society islands to the Savannah seamounts. Also shown (top left) is a "visually acceptable" interpretation which passes under rather than through individual bathymetric features. The volcanic edifices (light grey) are superimposed on a hot spot swell (dark grey) defined by a rise in the oceanic basement (bold line), which in turn rests on more regional seafloor depths (bold dashed line). None of regional depths (expanded profile) estimated by 400 km wide sliding spatial average filters (i.e., those of filter1d of GMT [*Wessel and Smith*, 1998]) reliably pass beneath the edifices. The mean "smears out" seamounts and is too shallow. A wider mean filter also proves unsatisfactory as the interaction (indicated by arrow) between Tahiti and the Savannah seamounts (grows). The median and the mode ignore some, though not all, of the height from the seamounts but pass through small-scale topography. The mode almost isolates Tahiti, but the accuracy with which it distinguishes the seamounts from the swell is poor. Bathymetric data is that of *Smith and Sandwell* [1997].

metric features that are superimposed on a regional. These two stages of underlining and identification are repeated along the profile.

[21] The flow chart on Figure 4 (bottom) shows a logical structure that approximates this process, but which may be followed computationally. Here, the bathymetric profile is an array of depths z_n (positive z is down), which occur at distances x_n from the start of the profile, and the point from which successive analytical cycles are initiated, x_i, passes along the profile (Figure 4 (top)).

[22] Each analytical cycle from x_i starts with a "search" for a topographic high of any morphology immediately along the profile from $x_{i=n}$. A search consists of incrementing search point x_s, of depth z_s, from $s = i$ until $z_s \geq z_i$ (middle left Figure 4) or $x_s - x_i \geq S_r$ or the end of the profile is reached. For a search that ends at $s > i + 1$ and satisfies the first condition, x_s has travelled up and down and a high, or more precisely the other side of a high, has been found. S_r is the "search range" (km) and limits the analysis to a particular scale range as no high is found if the second search termination condition is satisfied. Limiting S_r also increases computational efficiency. If either the search terminates at $s = i + 1$ (downward slope) or x_s reaches the end of the profile it is also considered that no high has been found. When no high is found a new search is begun immediately from $x_{i=i+1}$. When a topographic high between x_i and x_s is found, its shape is tested in a "morphological assessment."

[23] In the morphological assessment, a high is deemed inappropriate and fails if it does not comply with any of several shape restrictions or "tests" (Figure 4 (middle)). Upon failure a new search is initiated from $x_{i=i+1}$, otherwise a regional seafloor is linearly interpolated underneath the feature (i.e., between x_i,z_i and x_s,z_s) and a new search initiated from $x_{i=s}$ (middle right Figure 4).

[24] To ensure scale invariance during the morphological assessment the length of profile to be tested between x_i and x_s is normalized, i.e., scaled, into a unit box. The box extends around and just encompasses the horizontal and vertical limits of the section so that height and distance within the box can be thought of as fractions of the box dimensions, giving the box itself a size of 1.0 × 1.0. Thus

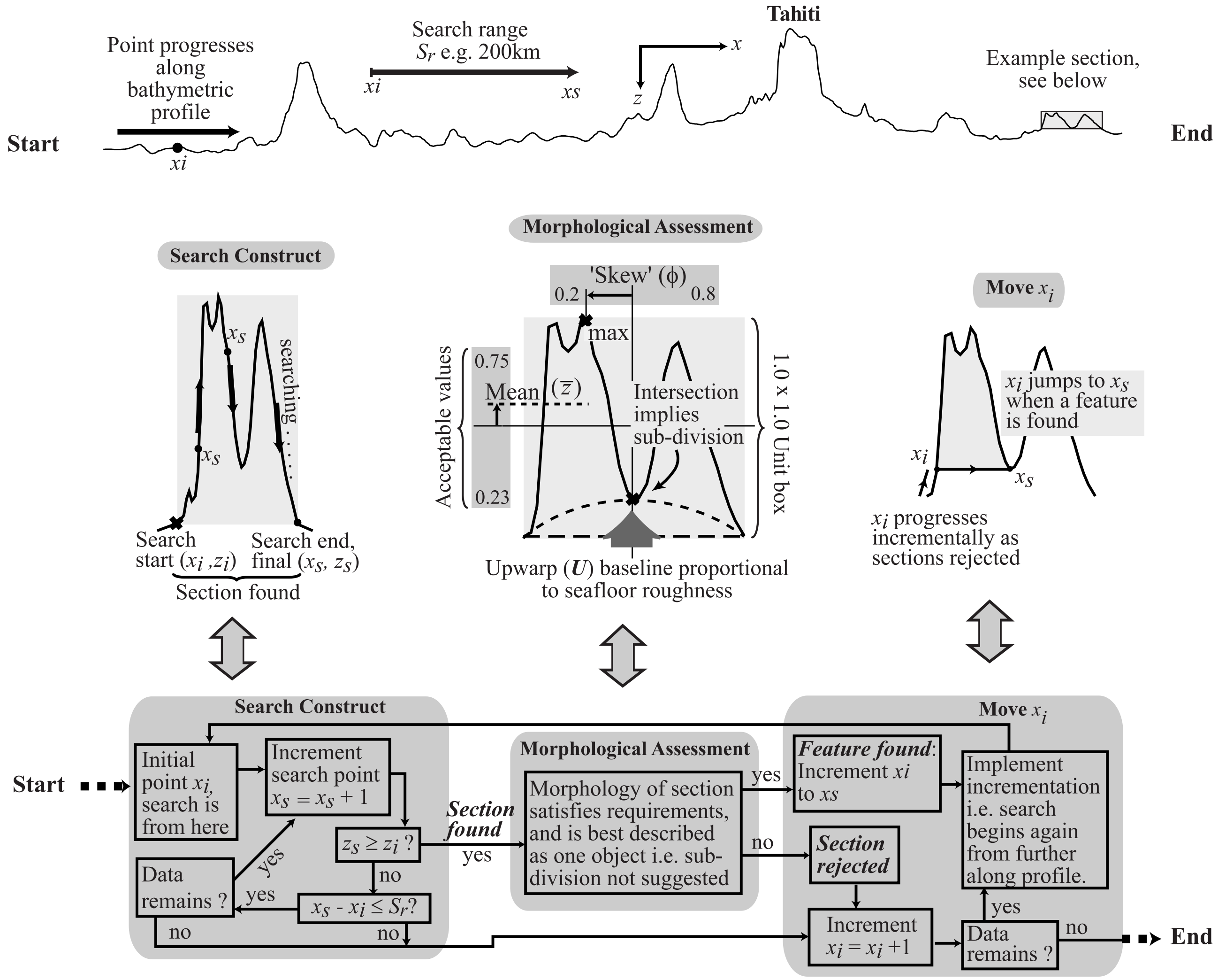

Figure 4. Algorithm schematic for MiMIC. MiMIC traverses bathymetric profiles (top) searching for, finding, morphologically assessing, accepting, or rejecting raised sections, then moving on. Simply, a search point x_s moves on from a start point x_i, and that search is over whenever the search point is deeper than the start point (“search construct,” left center). Thus x_i either moves incrementally downhill, or a rise is delimited for assessment (“morphological assessment,” center). Upon morphological rejection of a raised section, x_i moves incrementally uphill, while a morphologically acceptable (see text and Appendix A) feature is jumped underneath (right center). These stages are boxed grey in the flow chart (bottom), illustrated for an example section highlighted on the profile (top). Processing is controlled by four parameters; “search range” S_r, “skew” ϕ, mean height $\bar{z}$, and “up-warp” $\mathcal{U}$ (see text and Table 1). Profile is as Figure 3.

x_n where $i \leq n \leq s$ has a fractional distance (x_{frac}) along the section of $\frac{x_n - x_i}{x_s - x_i}$. $0 \leq x_{frac} \leq 1$. Similarly $0 \leq z_{frac} \leq 1$ is defined between $z_{\min}$ and $z_{\max}$.

[25] The shape tests are applied to this normalized section and are therefore scale-independent. We use three tests here: “skewness,” “average height,” and “up-warp.” A section fails the morphological assessment if ϕ (skew) and $\bar{z}$ (average height) do not fall within their empirically determined acceptable ranges, or if the “up-warp” test indicates that the section is better described as a subdivision into multiple geological features.

[26] Skewness (Figure 4 (middle)), ϕ, is the normalized position (x_{frac}) of the highest point within a section, and can have values 0 to 1. We have found that the rejection of skews outside the range $0.2 \leq \phi \leq 0.8$ (Table 1) helps to eliminate high sections that contain two or more features. This range was empirically established from the limits of single manually interpreted bathymetric features from ϕ versus $z_{\max}$ plots of cruise v3312 in the old NW Pacific, and cruise amph1 across the East Pacific Rise where there is coincident multibeam data (see data from RIDGE Multibeam Synthesis Project, grid sep500m, http://ocean-ridge.ldeo.columbia.edu).

[27] Average height (Figure 4 (middle)), $\bar{z}$, is a simple unweighted arithmetic mean of all data points within the box, and ranges between 0 and 1. We have found that the rejection of average heights outside the range $0.23 \leq \bar{z} \leq 0.75$ (determined as for ϕ) allow, for example, a steep-sided

Table 1. Parameters Used in MiMIC[a]

Control Parameters	Symbol	Value Pass 1	Value Pass 2
Search range, km	S_r	200	750
Skew	ϕ	0.2–0.8	inactive
Average height	$\bar{z}$	0.23–0.75	inactive
Up-warp	$\mathcal{U}$	active	inactive

[a] S_r controls the "search construct," and ϕ, $\bar{z}$, and $\mathcal{U}$ are criteria used in the "morphological assessment." "Inactive" indicates that morphological criteria have not been applied. Pass 1 or pass 2 indicates the stage of analysis (e.g., Figures 3 and 7). S_r for pass 1 was set because it is roughly the minimum distance required to isolate the largest ocean islands, e.g., Tahiti (Figure 3). S_r for pass 2 was set because significantly greater distances cause interactions between fracture zones, i.e., Marquesas and Austral (Figure 1). Parameter values are remarkably independent of scale, data type, and geographic location.

seamount to be distinguished from a wide gentle rise. Misleading geometries, due, for example, to a ship track that repeatedly crosses the center of a seamount, will also be suppressed.

[28] In the up-warp test (Figure 4 (middle)) a baseline, extending linearly between (x_i, z_i) and (x_s, z_s) shallowed by an "reasonable" up-warp $\mathcal{U}(x)$, is compared against "significant" points in the bathymetry in order to determine if the length of profile is best described as a single geological feature. If the up-warped baseline is shallower than any significant minima at the bottom of valley-like lows within a high, it is reasonable to place a regional through those minima and the section is best described as multiple features. It is therefore rejected and fails the test. The equation of $\mathcal{U}(x)$ and rigorous definition of significant and reasonable are given in Appendix A. Values for parameters controlling this test, $\mathcal{U}_m$ and $\mathcal{U}_c$ (see Appendix A), were determined by minimizing the r.m.s deviation between a manual interpretation and MiMIC's interpretation of the same 3 profiles used for ϕ & $\bar{z}$. All the parameterized morphological restrictions behave consistently between, data types and locations throughout the Pacific basin: e.g., cruises c1110, c1501, c1501, p7008, ew9106, and profiles extracted from gridded ship track data across the Hawaiian volcanic chain.

[29] Figure 3 compares the results of applying MiMIC to a bathymetric profile with the output of other filters. The figure shows that the Society Islands and the other constructional volcanic features (shaded light grey) along the profile are isolated by one pass of MiMIC, which uses S_r = 200 km, $\mathcal{U}$ = active, ϕ = 0.2–0.8, and $\bar{z}$ = 0.23–0.75. Moreover, when the profile is reanalyzed without these features with MiMIC (S_r = 750 km; $\mathcal{U}$, ϕ, and $\bar{z}$ inactive) the Society swell (shaded dark grey) is removed. Therefore the successive applications of MiMIC allow two categories of multiscale features to be removed.

[30] The sensitivity of the results of applying MiMIC along the Society Islands profile to the main controlling parameters is shown in Figure 5. The figure shows that reducing S_r, narrowing the permissible range of ϕ and $\bar{z}$, and increasing $\mathcal{U}_m$ increases the number of potential features that will be rejected by the morphological assessment. The resulting regional seafloor depth therefore shallows. Only large changes in ϕ, $\bar{z}$ and $\mathcal{U}$ from our preferred values, however, lead to any change in the interpretation. Moreover, the regional produced by MiMIC is insensitive to any increase in S_r above 200 km. We note though that the regional will still contain any localized deep areas.

4. Data Set

[31] Digital bathymetric data are available both as shipboard point data and as gridded values. Shipboard soundings are direct measurements and are therefore free of artifacts due to gridding such as those originating from the digitization of contour maps. However, their coverage in the superswell region is incomplete (e.g., 32.8% at 0.1° × 0.1° [*McNutt and Sichoix*, 1996]). Despite this, *Sichoix et al.* [1998] used all available shipboard soundings to determine depth-age, justifying it on the basis that there were data in nearly all 250 m × 3 Ma depth-age bins and that the distribution did not depend on whether only post-1973 (i.e., better navigated) or all available soundings were used. We question, however, this justification. The mere presence of data in a bin does not mean that they are spatially representative, and invariance to additional data does not preclude a systematic collection bias; for example, a bias toward the measurement of either shallow or deep areas.

[32] This point is illustrated in the region of the superswell (i.e., 160°–130°W, 3°–33°S) by a shipboard data set based on the GEODAS compilation [*NOAA*, 2003a]. The locations of data plotted onto a map show that shipboard data is preferentially collected around ports, and is therefore unrepresentatively shallow. This collection bias is reduced by spatially binning (e.g., blockmode of GMT *Wessel and Smith* [1998]) the data at 0.1° × 0.1° [*McNutt and Sichoix*, 1996]. However, given that the data set of *Smith and Sandwell* [1997] (shipboard control points in 4.3% of 0.1° × 0.1° spatial bins) contains information from satellite altimetry everywhere [see also *Smith and Sandwell*, 1994], any remaining bias is approximately quantified by a comparison between predicted depths extracted at the locations of spatial bins with and without GEODAS shipboard data. Bins containing shipboard data (35.7% of total) have predicted depths on average (mean) 213 m shallower than those without. This implies that a significant bias to shallow depths very likely remains. Therefore since it best avoids collection bias, we analyse gridded data, primarily the data set of *Smith and Sandwell* [1997]. However, we also use the shipboard data after 0.1° × 0.1° spatial binning and gridding with a bicubic spline (i.e., surface of GMT [*Smith and Wessel*, 1990]) at tensions T = 1 and T = 0 and, for completeness, GEBCO (IOC, GEBCO 1 min grid, see http://www.ngdc.noaa.gov/mgg/gebco) and ETOPO-5 [*NOAA*, 1988].

[33] Figure 6 compares the power spectra for the gridded data sets. At long wavelengths (wavelength, λ, >400 km) the spectra agree well. At intermediate wavelengths (approx. $100 < \lambda < 400$ km) the GEODAS shipboard grid with T = 0 appears to have slightly more power than GEBCO and ETOPO-5, suggesting additional data, but high tensions tend to reduce the power. At short wavelengths (approx. $20 < \lambda < 150$ km) however, the *Smith and Sandwell* [1997] predicted bathymetry grid has more power than GEODAS with T = 0, presumably due to the addition of small-scale features derived from satellite altimetry.

[34] In the central Pacific, sediments are typically less than a few hundred meters thick [*Jordahl et al.*, 1995; *McNutt*, 1998; *NOAA*, 2003b], which when their loading

effects are corrected for [*Marty and Cazenave*, 1989], affects regional seafloor depths "little" [*McNutt*, 1998] i.e., mostly ~100 m [*Schroeder*, 1984], with local exceptions. Thus as previous workers [*Levitt and Sandwell*, 1996; *McNutt and Sichoix*, 1996; *Sichoix et al.*, 1998; *McNutt*, 1998] we forego this correction.

5. Application to the South Pacific

[35] We have applied MiMIC to gridded bathymetric data sets over a large region of the South Pacific ocean (160°–117°W, 3°–33°S). The region includes the superswell as defined by *McNutt and Fischer* [1987] and an area to the east (Figure 1). We did not analyse the bathymetry to the west of 160°W because of the poor age control in this region [*Müller and Roest*, 1997].

[36] Although MiMIC was initially conceived to process data along ship tracks, we use profiles that have been interpolated from gridded bathymetries. The profiles trend in 4 directions forming a mesh across the grid (example inset on Figure 7b). Sets of profiles in the N–S and E–W directions were separated by 0.2° and the NW–SE and NE–SW lines by 0.35°. Bathymetric data was extracted every 3 km, and 2° of surrounding data was used as a buffer to avoid possible edge effects. The "regional" depths output by MiMIC along individual profiles within a set were combined by gridding with a tensioned (T = 0.85) bicubic spline (surface [*Smith and Wessel*, 1990]), and the deepest value of the 4 gridded sets at any point taken to be the output regional depth. Thus morphologically selected features narrower than S_r in any direction processed were isolated. The simple geometry of the profiles was chosen for convenience and because any artifacts generated by the processing will show up as lines and have an azimuth in multiples of 45°, thus making them easy to identify (e.g., Figure 7c).

[37] The bathymetry of the South Pacific was analysed twice sequentially using MiMIC, resulting in its separation into 3 components (e.g., Figures 7a–7c). The first pass with S_r = 200 km, $\mathcal{U}$ = active, ϕ = 0.2–0.8, and $\bar{z}$ = 0.23–0.75 (Table 1) isolated seamounts, oceanic islands and other small-scale features (Figure 7a). This is despite the possibility of some of these features being flanked by water-filled flexural moats. MiMIC might be expected to link up adjoining flexural moats. This does not appear to have happened, however (Figure 7a), suggesting that most moats are filled (see also Figure 3). Topography associated with short-wavelength (<200 km) "Haxby" [*Wessel et al.*, 1996] gravity lineations [*Haxby and Weissel*, 1986; *Buck and Parmentier*, 1986; *McAdoo and Sandwell*, 1989; *Fleitout and Moriceau*, 1992] is not visible and is therefore, if present, of small amplitude. We speculate that the use of

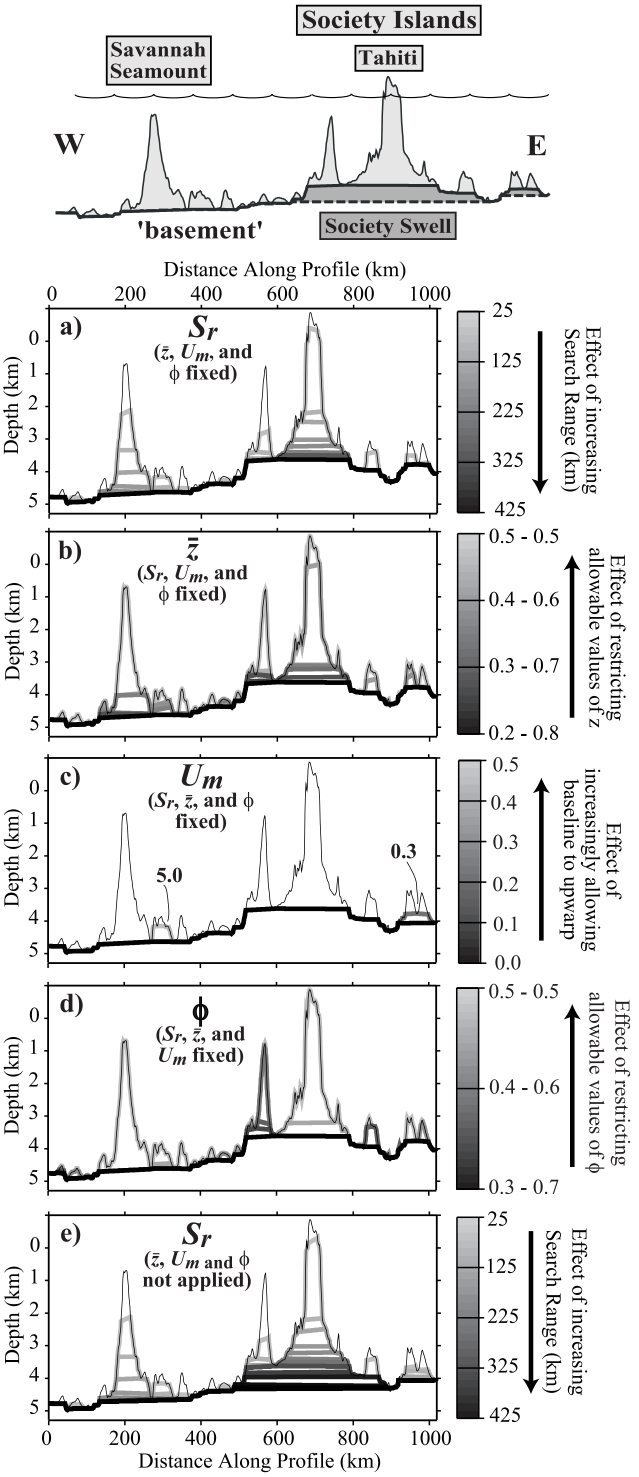

Figure 5. Sensitivity of the interpretations produced by MiMIC to the values of the control parameters $\bar{z}$, $\mathcal{U}_m$, ϕ, and S_r used (Table 1). Either restricting the ability of the search construct (middle left Figure 4) to find potential features by restricting S_r or making the morphological tests increasingly restrictive, causing more highs to be rejected, leads to a shallower regional depth. (a) Variable S_r. Grey lines are regional depths, with S_r in 25 km steps. Larger S_r is darker. Results for $S_r \geq 200$ km are identical. (b, d) Range of $\bar{z}$ and ϕ, respectively, varied symmetrically about 0.5. Steps displayed ±0.025. Note that the interpretation varies little from that of our preferred ranged (thick black line) until the ranges considerably changed from our preferred ones. No change in interpretation occurs for wider ranges than $0.3 \leq \bar{z} \leq 0.7$ and $0.35 \leq \phi \leq 0.65$. (c) Variable $\mathcal{U}_m$ (defined in Appendix A). Steps 0.025. $\mathcal{U}_m$ must be changed by either ×1/2 or ×10 to alter the interpretation from that of $\mathcal{U}_m$ = 0.5, our preferred value. (e) As in Figure 5a, except morphological tests were not applied. Base of swell is now found. No change S_r > 425 km. Profile is as Figure 3.

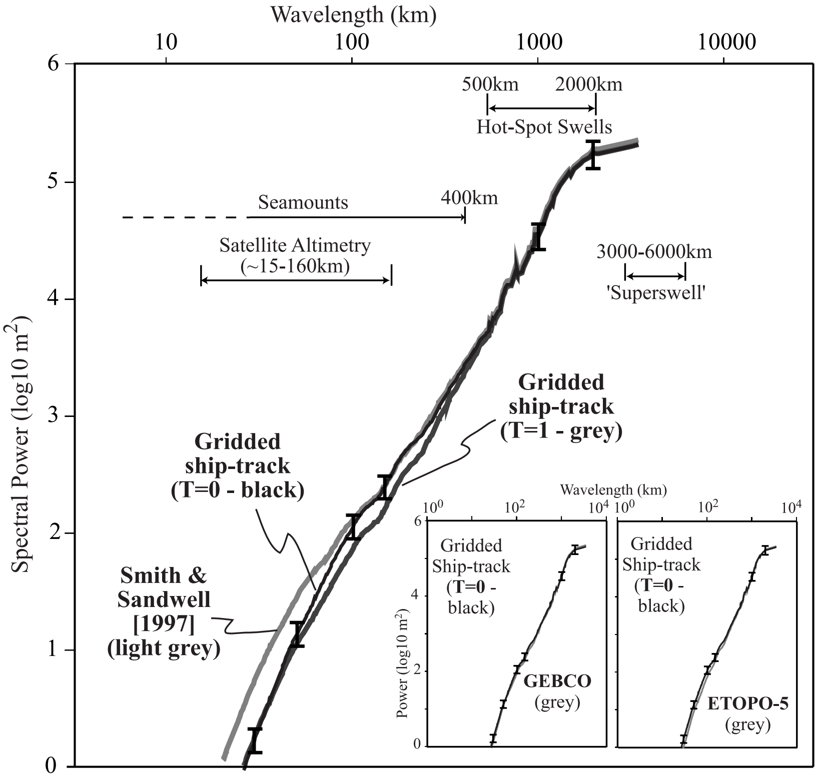

Figure 6. Comparison of the power spectra of the *Smith and Sandwell* [1997] predicted bathymetric data set and grids of spatially binned (i.e., 0.1° × 0.1° blockmode of GMT [*Wessel and Smith*, 1998]) and interpolated (i.e., surface of GMT [*Smith and Wessel*, 1990]) ship track data. The analysis area is 160°–117°W, 3°–33°S. T = 0 and T = 1 indicate untensioned and tensioned bicubic spline interpolations, respectively. At long wavelengths ($\lambda \geq 400$ km), corresponding approximately to hot spot swells and the superswell, the data sets agree. However, at short wavelengths (approximately $50 < \lambda < 150$ km), corresponding approximately to seamounts and ocean islands, there is more spectral power in the *Smith and Sandwell* [1997] data set than the ship track grids. Insets compare the power spectra of the ship track data gridded at T = 0 to GEBCO and ETOPO-5. Spectra calculated from Mercator projection of the data resampled at a 10 km spacing using Thompson multiple-Slepian-taper spectral analysis [*Simons et al.*, 2000]. Nine tapers were used. Spectra displayed are radial arithmetic means of directional wave number estimates, each of which is a jackknifed [*Thomson and Chave*, 1991] estimate of the mean spectra generated by the individual tapers. Similarly, the ±1 standard deviation error bars are radial means of jackknifed estimates of the standard deviation. Prediction of bathymetry using satellite altimetry is possible in the wavelength range $15 < \lambda < 150$ km [*Smith and Sandwell*, 1997]. Superswell size is from *McNutt* [1998], and size ranges of seamounts and hot spot swells are eyeballed from bathymetric charts, e.g., GEBCO.

wavelength based (e.g., bandpass) analysis in previous studies may explain this apparent discrepancy.

[38] The second pass (Figure 7b) isolates larger features such as localized [*Sichoix et al.*, 1998] hot spot swells (e.g., Society) and oceanic plateaus (e.g., Tuamotu). Since the general shape of these larger-scale features is difficult to collectively parameterize, $\mathcal{U}$, ϕ, and $\bar{z}$ were not applied on this pass, but S_r was set to 750 km in order to avoid the possibility of MiMIC linking up fracture zones troughs (e.g., Marquesas and Austral). Topography previously associated with intermediate-wavelength (~1000 km) geoid anomalies [*Cazenave et al.*, 1992] corresponds spatially to identifiable features (i.e., swells and plateaus) and so, if present, is difficult to distinguish.

[39] Figure 7c shows the depth anomaly derived by subtracting the expected bathymetry based on the cooling plate model of *Parsons and Sclater* [1977] from the regional bathymetry that remains after two passes of MiMIC. The figure shows that without its superimposed small-scale bathymetric features (Figures 7a and 7b), seafloor depths in the superswell region (160°–130°W) [*McNutt and Fischer*, 1987] are mostly anomalously shallow. The shallowing is best developed between latitudes 12°–26°S, and in accord with previous tentative suggestions [*Sichoix et al.*, 1998] that the anomaly is not bounded by the Marquesas and Austral fracture zones.

[40] Figure 8 compares the regional bathymetry derived using MiMIC for the region: lat. 12°S–26°S and long. 160°W–117°W to the expected bathymetry based on a cooling plate model [*Parsons and Sclater*, 1977]. The plot shows that young seafloor subsides relatively slowly at a rate of about 218 m Ma$^{-1/2}$, in agreement with results of previous studies [*Cochran*, 1986; *Marty and Cazenave*, 1989; *Levitt and Sandwell*, 1996; *McNutt*, 1998]. We concur

with *Levitt and Sandwell* [1996] that a small depth (<+200 m) anomaly is present over crust of ages 15–35 Ma [*Levitt and Sandwell*, 1996]. However, we disagree with them that this is evidence against the existence of a superswell.

[41] The most important result, shown in Figure 8, is that the large-scale seafloor trend deduced using MiMIC is monotonic and continuous between young (<5 Ma) and old (>110 Ma) seafloor, which are deeper and shallower than expected [*Parsons and Sclater*, 1977], respectively. The maximum deepening is about 500 m near the EPR crest, in accord with previous results [*Cochran*, 1986; *Levitt and Sandwell*, 1996] (see Figures 2 and 9). The maximum shallowing is 712 ± 66 m (1 s.d) at 98 Ma, not 1300 m at ~65 Ma [*McNutt and Sichoix*, 1996], and there is no evidence of a significant seafloor rise between 40 and 80 Ma as described by *McNutt and Sichoix* [1996] and *Sichoix et al.* [1998].

6. Origin of the Depth Anomalies

[42] The analysis using MiMIC suggests that regional seafloor depth in the EPR-superswell region (160°–117°W, 12°–26°S) subsides monotonically with increasing thermal age of the oceanic lithosphere. We find no evidence west of the EPR for a isolated region where the subsidence is reversed and the seafloor uplifted as suggested by *McNutt and Fischer* [1987], *McNutt and Sichoix* [1996], *Sichoix et al.* [1998], and *McNutt* [1998] (Figure 8). Rather, the subsidence of the seafloor from the relatively deep EPR through the relatively shallow superswell appears continuous and "plate-like." Because of this continuity we link the superswell to the EPR and postulate that the same geodynamic processes act upon both old seafloor in the superswell region and young seafloor at the EPR, forming an "EPR-superswell system."

6.1. Variations in Crustal Thickness

[43] The most obvious source of depth anomalies are crustal thickness variations. Unusually thin crust, for example, would cause deeper than expected seafloor while thick crust is indicative of shallower bathymetry. There is evidence from seismic refraction profile data that the Marquesas swell [*Caress et al.*, 1995; *McNutt*, 1998] and the Tuamotu Plateau [*Talandier and Okal*, 1987; *Ito et al.*, 1995; *McNutt*, 1998; *Patriat et al.*, 2002] are underlain by thickened crust and correlate with unusually shallow seafloor. Away from such features, however, there is no evidence that the crust thins or thickens significantly across the EPR-superswell system. To the west (proximal to the Marquesas Swell and NW Tuamotu Plateau) the oceanic crust is 6 ± 1 km [*Caress et al.*, 1995; *Ito et al.*, 1995; *McNutt*, 1998] while to the east, near the EPR, it is 4.8–

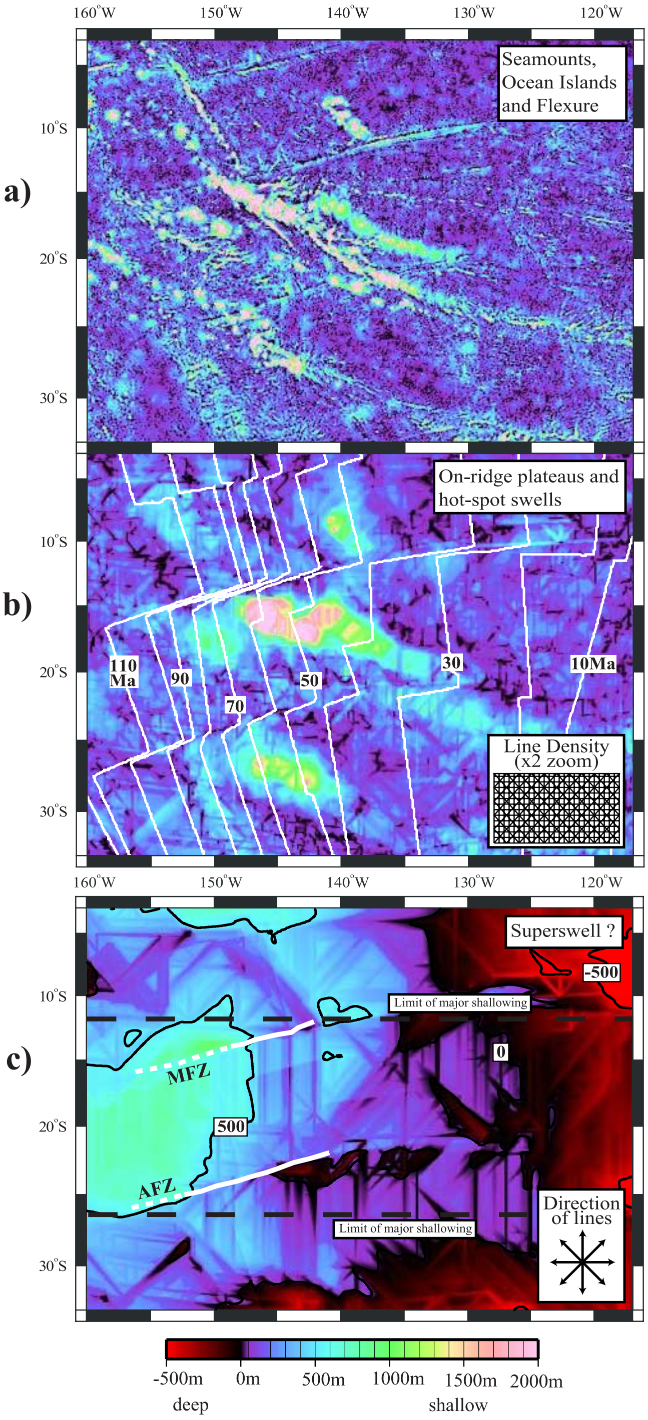

Figure 7. Application of MiMIC to the predicted bathymetry of *Smith and Sandwell* [1997] in the South Pacific. (a) Pass 1 of MiMIC with $S_r = 200$ km, $\phi = 0.2–0.8$, $\bar{z} = 0.23–0.75$, $\mathcal{U}$ = active (see Table 1) isolates oceanic islands, seamounts, fracture zone ridges, and troughs, and other small-scale features. The color scheme indicates height isolated. (b) Pass 2 of MiMIC, with $S_r = 750$ km, but ϕ, $\bar{z}$ and $\mathcal{U}$ = inactive isolates large-scale features such as oceanic plateaus and hot spot swells. (c) The residual depth anomaly obtained by subtracting what remains of the bathymetry after two passes from the predictions of the cooling plate model of *Parsons and Sclater* [1977]. Artifacts are parallel to the direction of the profiles used (inset). White lines are Marquesas Fracture Zone (MFZ) and Austral Fracture Zone (MFZ). Black dashed lines are the latitudes within which substantial (>500 m) shallowing (green shades) is well developed in the west. Differences in interpretation caused by doubling or halving data sampling (points per kilometer along profiles) or mesh spacing (separation between profiles) is small scale, appears randomly distributed, and affects the average height isolated little, i.e., by ~±5–10 m.

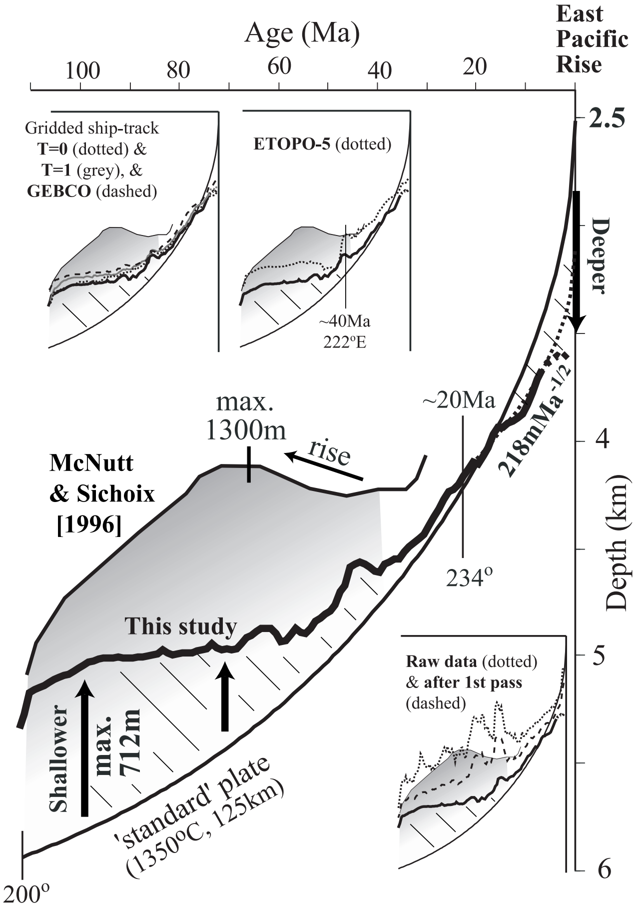

Figure 8. Plot of large-scale bathymetry against age of the seafloor in the South Pacific. The thick solid line shows the regional bathymetry after two passes of MiMIC over the data set of *Smith and Sandwell* [1997]. The thin solid line shows the expected depth based on the standard cooling plate model. The thin solid line with grey shade shows the depth obtained by *McNutt and Sichoix* [1996] from modal analysis. Note that the regional bathymetry deepens monotonically, if slowly ~218 m Ma$^{-1/2}$, from a relatively deep EPR crest. The trend appears continuous between young and old seafloor. Contrary to the results of *McNutt and Sichoix* [1996] (trend as in Figure 2) and *Sichoix et al.* [1998], there is no significant decrease in ocean depth for ages of oceanic crust between 40 and 80 Ma. Other data sets show a similar trend (inset top). Raw data and the remaining bathymetry after MiMIC's first pass are shown for comparison (inset bottom). The trends shown are running means of data for the latitudes where the shallowing is most pronounced (Figure 7), i.e., 12°–26°S.

6.3 km (data at 15°55′S and 17°15′S) [*Canales et al.*, 1998] or 6.11 ± 0.14 km (at 14°S) [*Grevemeyer et al.*, 1998].

6.2. Compositional Buoyancy

[44] Another possible contributor to oceanic depth anomalies is compositional buoyancy due to basalt extraction [*Jordan*, 1979; *Robinson*, 1988]. Melting depletes fertile mantle in garnet and raises the MgO/FeO ratio of the residuum, which becomes less dense [*O'Hara*, 1975; *Boyd and McCallister*, 1976; *Oxburgh and Parmentier*, 1977]. This effect can be parameterized as $\Delta\rho = \rho_0\beta f$ where f is the mean extent of melt extraction from a column of height h_d, $\beta = 0.06$, and ρ_0 is the density of the mantle (Table 2) [*Phipps-Morgan et al.*, 1995; *McNutt*, 1998]. A column-integrated buoyancy, b, is therefore $b = \rho_0\beta F h_d$. Since $h_d = h_b/f$, where h_b is the thickness of extracted basalt, then it follows that $b = \rho_0\beta h_b$. Divided by the effective density of seafloor topography, i.e., $\rho_c - \rho_w$ (Table 2), this gives an Airy-type isostatic shallowing of $0.1128h_b$ or ~1/9thh_b [*McNutt*, 1998].

[45] For seamounts, however, *McNutt* [1998] notes that the amount of erupted basalt observed as edifices at the surface must be multiplied by a factor of 6 to include basaltic material infilling the flexural moat [*Filmer et al.*, 1994; *Wolfe et al.*, 1994], and the total must be doubled again in cases where magmatic material underplates the crust [*Caress et al.*, 1995]. Thus shallowing of the seafloor due to compositional buoyancy (Figure 9a) may be as much as ~12 × 1/9th = ~4/3rd of the observed seamount height (Figure 7a). This uplift (Figure 9a) is almost sufficient in magnitude to explain the large-scale depth anomaly (Figure 9b), however it is distributed differently in space. Seamount volume, for example, distinctly decreases west of 150°W, while the depth anomaly does not. Thus the large-scale depth anomalies are not due to compositionally less dense material vertically below them in the lithosphere. If, however, chemical buoyancy within the asthenosphere [e.g., *Phipps-Morgan et al.*, 1995; *Manglik and Christensen*, 1997; *Ribe and Christensen*, 1999] can endure for long periods of time, previous volcanic episodes (e.g., the events that formed the on-ridge Cretaceous oceanic plateaus) may also contribute to uplift. Thus we cannot entirely discount this mechanism.

6.3. Lithospheric Reheating

[46] Reheating and consequent thinning of the lithosphere [*Detrick and Crough*, 1978], perhaps by a hot upwelling plume [*Dietz and Menard*, 1953; *Morgan*, 1971; *Clouard and Bonneville*, 2001], has been widely invoked to explain isolated topographic swells associated with recent volcanism such as Hawaii and Cape Verde. However, it is difficult to see how this mechanism could explain depth anomalies in the EPR-superswell system. Lithospheric reheating at, for example, the Marquesas, Society, Austral, and Pitcairn hot spots [*Crough*, 1978; *Menard and McNutt*, 1982] would reduce density and cause uplift, but the depth anomaly would not be correctly located [*McNutt and Fischer*, 1987]. The increasingly likely contact of the lithosphere as it ages with randomly distributed reheating events [*Smith and Sandwell*, 1997] could produce a correctly distributed depth anomaly. However, the volcanic "trails" expected from these events are not observed in the bathymetry data (Figure 7b). Besides, T_e [*Filmer et al.*, 1993; *Goodwillie and Watts*, 1993; *McNutt et al.*, 1997; *McNutt*, 1998] and surface heat flow [*Stein and Abbott*, 1991] appear normal in the superswell region, not lowered and raised respectively as would be expected for a widespread reheating event.

6.4. Cooling Plate Models

[47] The monotonic subsidence of the EPR-superswell system is similar in form to the predictions of the standard

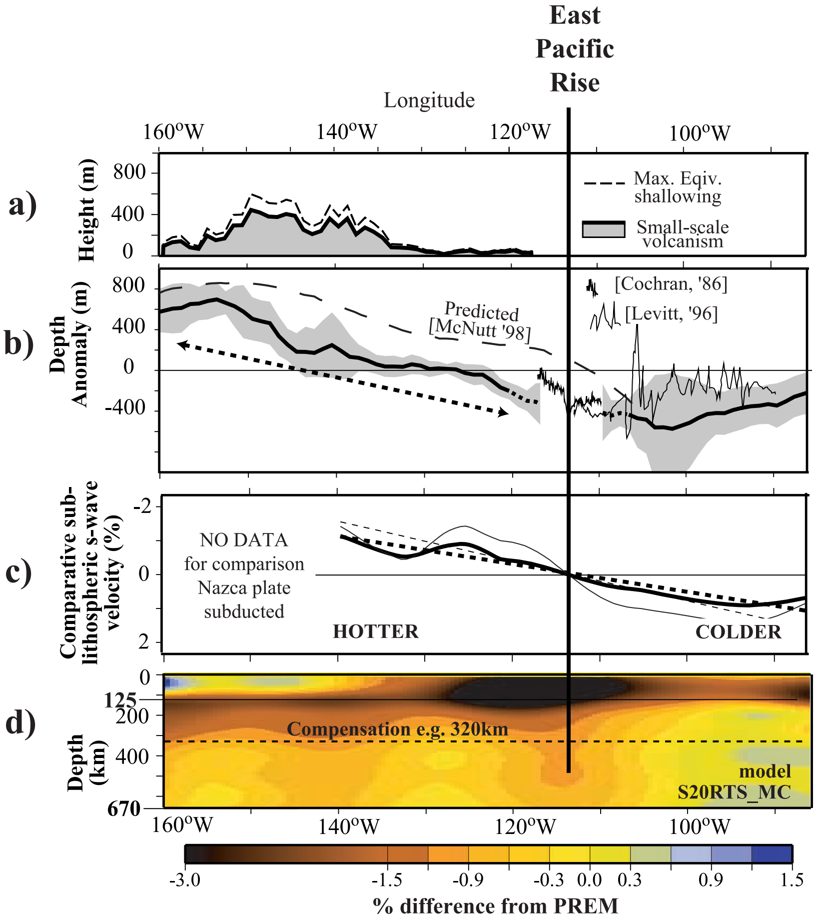

Figure 9. Comparison of large-scale regional depth anomalies to small-scale volcanism and sublithospheric shear wave velocities in the South Pacific superswell–EPR system. (a) Bold line is the mean height of small-scale intraplate volcanism (V_s) between 12° and 26°S. Features used to calculate this are from the bathymetry of *Smith and Sandwell* [1997] after the first pass of MiMIC (Figure 7a), but morphologies ≤500 m were excluded. The dashed line is a maximum estimate of the basement shallowing associated with this volcanism ($\mathcal{S}$) [*Jordan*, 1979]. $\mathcal{S} = \frac{4V_s}{3}$ [*McNutt*, 1998] (see text). (b) The bold line is the mean large-scale depth anomaly for the bathymetry of *Smith and Sandwell* [1997] (i.e., difference between depth after two passes of MiMIC and the cooling plate model of *Parsons and Sclater* [1977]) in the superswell-EPR system between 12° and 26°S. Grey shading is $\pm 2\sigma$ (standard deviations) about this mean. The gap around EPR exists as profiles cannot cross the EPR (MiMIC would remove part of it), and profile meshes are over geometrically regular areas. Thin lines show other depth data digitized from *Cochran* [1986, Figure 5] and *Levitt and Sandwell* [1996, Figure 5f]. The dashed line is an example dynamic topography produced by converting velocity anomalies to temperature anomalies and assuming a viscosity structure [*McNutt*, 1998]. (c) The bold line is the difference between sublithospheric (125–670 km) vertically averaged S wave velocities [*Ritsema et al.*, 1999] at 19°S (as shown in Figure 9d) under a lithosphere of the same age either side of the EPR. The comparison helps to remove any lithospheric effects which may be present below 125 km due to the vertical resolution of the tomography, which will be similar for both plates. The linear trend (dashed line) is fitted with filter1d [*Wessel and Smith*, 1998]. The fine line is for 125–325 km. All nondigitized trends are means for each 1° longitude.

cooling plate model [*Parsons and Sclater*, 1977]. However, while a hotter, thinner, plate (1450°C, 95 km) [*Stein and Stein*, 1992] (shown Figure 10), or (1385°C, 75 km) [*McNutt and Fischer*, 1987], could explain a shallowing of the seafloor at older ages they predict too rapid a subsidence at young ages [*McNutt*, 1998]. In particular, the slow subsidence rate of 218 m $\mathrm{Ma}^{-1/2}$ [*Levitt and Sandwell*, 1996] on the western flank of the EPR may be

Table 2. Assumed Values of Lithospheric Parameters

Parameter	Symbol	Value
Coefficient of thermal expansion, °C	α	3.2×10^{-5}
Thermal diffusivity, $m^2\ s^{-1}$	κ	0.8×10^{-6}
Mantle density (at 0°C), kg m^{-3}	ρ_0	3330
Water density (at 0°C), kg m^{-3}	ρ_w	1030
Crustal density, kg m^{-3}	ρ_c	2800

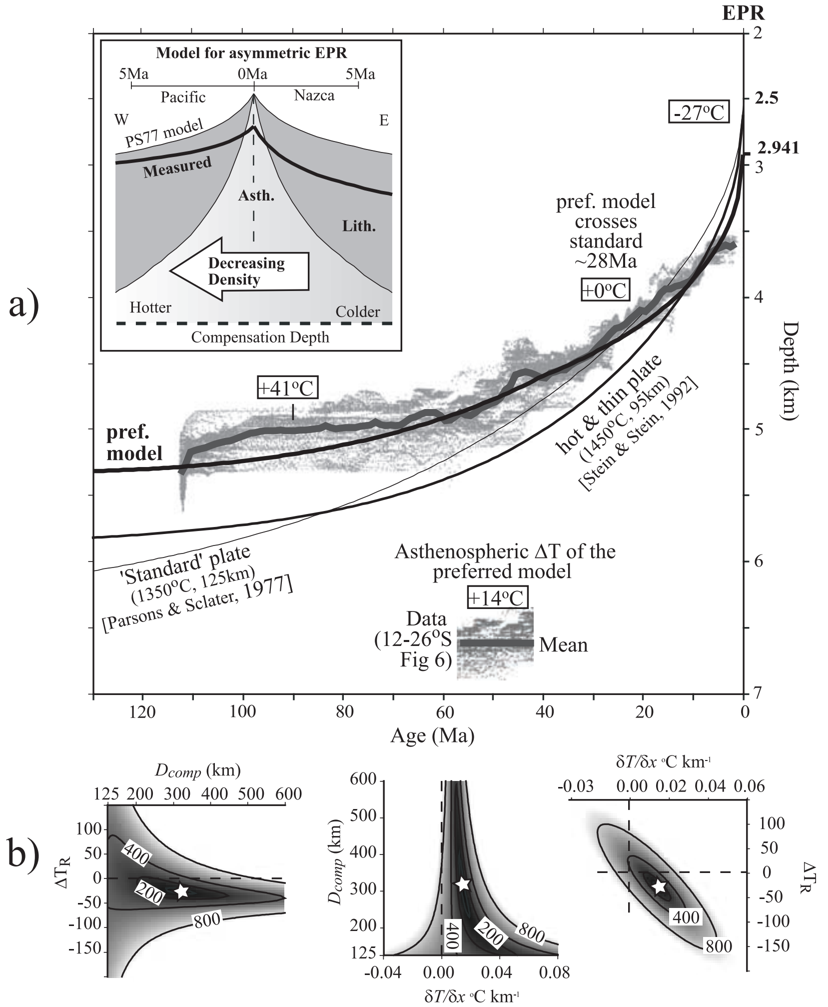

Figure 10. Comparison of the MiMIC processed bathymetry to the predictions of theoretical lateral temperature gradient models. (a) The thick dark grey line is a mean of each 1° of longitude of regional bathymetry after two passes of MiMIC between 12° and 26°S (light grey dots). The heavy black line is bathymetry predicted by our preferred model (see text); selected asthenospheric temperature anomalies are shown. Thinner lines are the predictions of cooling plate models [*Parsons and Sclater*, 1977; *Stein and Stein*, 1992]. Note that in contrast to our model, these subside too quickly and remain too deep. The inset illustrates the model of *Cochran* [1986]. (b) Contoured plots of rms misfit between model and data, illustrating the sensitivity of parameters ΔT_R (temperature anomaly at EPR), $\frac{\delta T}{\delta x}$ (lateral sublithospheric temperature gradient), and D_{comp} (depth of isostatic compensation) which describe our model. Positive $\frac{\delta T}{\delta x}$ indicates temperatures increasing to the west. Spreading half-rates used are from the age data of *Müller and Roest* [1997]; 0–10 Ma = 74.9 mm a^{-1} (i.e., mm per annum), 10–40 Ma = 66.9 mm a^{-1}, and 40–110 Ma = 41.3 mm a^{-1}.

generated by a half-space cooling from a temperature of 830°C (constants in Table 2), while a 115 km thick cooling plate with a basal temperature of 920°C best fits the regional bathymetry deduced using MiMIC. Both these estimates, however, are unrealistically cool in comparison to mantle potential temperatures (T_p) expected from petrological considerations (T_p = 1350°C [*McKenzie*, 1984], T_p = 1280°C [*McKenzie and Bickle*, 1988]).

7. Discussion

[48] The above considerations suggest that models based on crustal thickness variations, reheating by mantle plumes, compositional buoyancy, and variations in parameters of the cooling plate model are unlikely to account for the depth anomalies in the EPR-superswell system.

7.1. A Lateral Temperature Gradient Model

[49] One possibility is that the depth anomalies are caused by lateral density gradients in the sublithospheric mantle. *Cochran* [1986], for example, interpreted the asymmetry in the subsidence rate at the EPR crest in terms of a linear lateral sublithospheric temperature increasing to the west at about 0.1°C km^{-1}. A temperature gradient is also suggested by the approximately linear trend in the sublithospheric (125–670 km) S wave velocity structure of *Ritsema et al.*

[1999] (Figures 9c and 9d) and in the asymmetric distribution of volcanic features across the EPR [*Scheirer and Forsyth*, 1998].

[50] The lateral temperature gradient model of *Cochran* [1986] was applied by him to relatively young (i.e., <5 Ma) oceanic lithosphere at the EPR rise crest. Our bathymetric analysis suggests that the region of depth anomalies extends beyond the rise crest to its flanks. We have therefore reexamined the *Cochran* [1986] model and its applicability to the entire EPR-superswell system.

[51] The model we use is based on a cooling plate with a zero age depth of 2500 m, a basal temperature, T_0, of 1350°C, and a thermal thickness of 125 km which overlies an asthenosphere with a laterally varying temperature and, hence, density structure. We first isostatically balance the seafloor depths predicted by the cooling plate model against a column at the ridge crest, assuming a uniform density asthenosphere. Mantle density varies linearly with temperature as $(1 - \alpha T)\rho_0$ (constants in Table 2) such that the plate has an average density of $\rho_{av} = (1 - \alpha T_0/2)\rho_0$ while the asthenosphere has a density of $\rho_{asth} = (1 - \alpha T_0)\rho_0$. This yields a lithospheric thickness that varies as a function age, shown dark grey on the inset of Figure 10. We next introduced a lateral temperature, and hence density ($\rho = \rho_0(1 - \alpha T)$), variation in the asthenosphere and calculated the combined buoyancy effect on the seafloor of temperature variations in the asthenosphere and reheating of the lithosphere. The temperature structure associated with the reheating is assumed to be that of a half-space which is heated by a temperature gradient on its boundary, following a solution by *Carslaw and Jaeger* [1959]. We found that there is little error (<0.5%) associated with this assumption for small (i.e., ~0.010°C km^{-1}) temperature gradients.

[52] Figure 10 shows a comparison of the regional bathymetry after two passes of MiMIC to the calculated bathymetry based on a lateral temperature gradient model. The model is parameterized in terms of a ridge temperature anomaly (δT_R), a sublithospheric temperature gradient ($\delta T/\delta x$), and a depth of isostatic compensation (D_{comp}). Figure 10a shows the bathymetry associated with the preferred model, which has $\delta T_R = -27$°C, $\delta T/\delta x = 0.014$°C km^{-1}, and $D_{\text{comp}} = 320$ km. The model fits the regional bathymetry well, and in contrast to the predictions of global cooling plate models [*Parsons and Sclater*, 1977; *Stein and Stein*, 1992], accounts for both the unusually deep seafloor at the EPR and the shallow seafloor in the superswell region. Figure 10b shows the sensitivity of the fit to variations in the model parameters.

[53] The best fit model parameters in Figure 10b are consistent with other geophysical constraints. At the EPR the oceanic crust is 1–2 km thinner [*Canales et al.*, 1998; *Grevemeyer et al.*, 1998] than the global average of 7.1 ± 0.8 km [*White et al.*, 1992] which suggests a 19°–41°C reduction in ridge crest mantle potential temperature [*McKenzie*, 1984, Figure 12], compared to our estimate of 27°C. Beneath the Superswell, slow seismic velocities [*Hager and Clayton*, 1989] suggest to *McNutt and Fischer* [1987], via the scaling law of *Creager and Jordan* [1986], temperatures elevated by ~40°C. This number is similar to our estimate of 41°C. We note that these temperature anomalies are small and are unlikely to significantly modify the value of T_e and surface heat flow from that expected for oceanic crustal age [*McNutt*, 1998]. This is consistent with observations that T_e and surface heat flow are "normal" in the superswell region [*Stein and Abbott*, 1991; *Filmer et al.*, 1993; *Goodwillie and Watts*, 1993; *McNutt et al.*, 1997].

[54] The depth of compensation, D_{comp}, is probably the poorest constrained of our model parameters. Nevertheless, our preferred D_{comp} coincides with a transition in seismic velocity anomalies to a lower amplitude below ~320 km [*Montagner and Tanimoto*, 1991; *Ritsema et al.*, 1999] (Figure 9d). In this simple static model, however, density variations above D_{comp} are entirely compensated at the surface, which may not be the case if, for example, vertical motions occur in a viscously stratified fluid mantle [e.g., *McNutt*, 1998]. Thus D_{comp} may not actually be the depth of a physical transition, but rather an approximation of a more complex behavior.

7.2. A Pressure-Driven Flow Model

[55] Another possibility, tested in the vicinity of the EPR, is that the depth anomalies are caused by a lateral west to east across-axis flow driven by excess far-field pressure [*Toomey et al.*, 1998; *Conder et al.*, 2002]. Only these models satisfactorily explain the observations of the MELT experiment [*Forsyth et al.*, 1998b], which are asymmetry in mantle seismic velocity [*Forsyth et al.*, 1998a; *Toomey et al.*, 1998], seismic velocity anisotropy [*Wolfe and Solomon*, 1998], and electrical structure [*Evans et al.*, 1999] at 17°S on the EPR.

[56] The models, however, purely involve forcing material into an "asthenospheric" [*Morgan and Smith*, 1992] channel and do not include buoyancy forces or a temperature gradient. They cannot therefore explain the observed large-scale trend in sublithospheric seismic velocities (Figures 9c and 9d), nor account for the temperature gradient implicit in a flow driven by "hotspots in the superswell region" [*Toomey et al.*, 1998] which, by observation [*Niu et al.*, 2002] and implication, are probably hot. The most likely explanation of the EPR-superswell system is probably therefore some combination of the thermal-buoyancy and pressure-gradient models.

7.3. Synthesis and Implications

[57] Across-axis flow is necessary to replicate the anomalies observed by the MELT experiment [*Toomey et al.*, 1998; *Conder et al.*, 2002] as "no linear temperature gradient alone adequately matches both the asymmetric subsidence and the asymmetric seismic and conductivity structure" [*Conder et al.*, 2002]. However, the driving force for flow from the superswell region is generated by primarily thermal density differences, which are required to reproduce the linearly increasing seismic velocities up to and across the EPR. Thus a coupled temperature and driving-pressure gradient probably extends across the EPR-superswell system.

[58] In such a model, both buoyancy and the forcing of material into a channel contribute to topography, so temperatures estimated by the thermal gradient model are maximum estimates. The continued effect of buoyancy forces across the EPR-superswell system causing the hot material to "spread out" and flow sideways will also reduce the forcing required making it more explainable

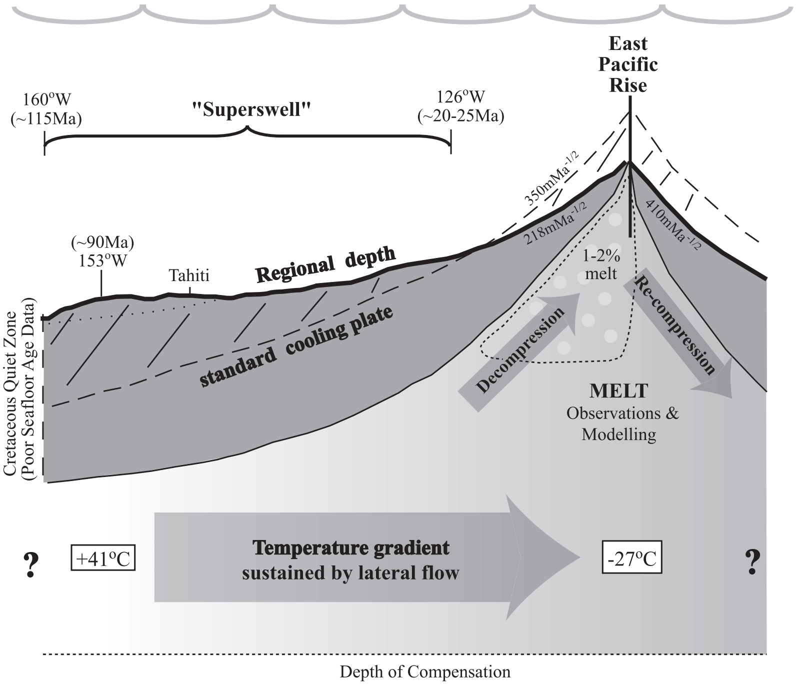

Figure 11. Illustration of a model to explain the regional bathymetry of the EPR-superswell system. The heavy solid line shows regional bathymetry that subsides continuously and monotonically, but slowly, from a deep EPR. With age it becomes anomalously shallow. Depth anomalies (hashed lines) [*Menard*, 1973] are with respect to the standard cooling plate model [*Parsons and Sclater*, 1977] (dashed line). Asymmetric subsidence at the EPR [*Cochran*, 1986; *Levitt and Sandwell*, 1996] is replicated by the buoyancy effects [*Cochran*, 1986] of a lateral asthenospheric temperature gradient (variable grey shading) between the base of the plate and the depth of isostatic compensation (short-dashed horizon). Temperature anomalies implied by the gradient of our preferred model (shown for 0 and 90 Ma) are consistent with crustal thickness [*McKenzie*, 1984; *White et al.*, 1992; *Canales et al.*, 1998; *Grevemeyer et al.*, 1998], tomography [*McNutt and Fischer*, 1987; *McNutt*, 1998; *Ritsema et al.*, 1999], and asymmetrical volcanism at the EPR [*Scheirer and Forsyth*, 1998]. Geochemical data [*Woodhead and Devey*, 1993; *Janney et al.*, 2000] and numerical modeling [*Toomey et al.*, 1998; *Conder et al.*, 2002] of the observations of the MELT experiment [*Evans et al.*, 1999; *Forsyth et al.*, 1998b; *Toomey et al.*, 1998; *Webb and Forsyth*, 1998] suggest that a pressure gradient is also present and that the temperature gradient is sustained by lateral flow (wide arrow).

by the pressure head under a 700 m rather than a 1300 m superswell anomaly.

[59] Our observations and modeling of the subsidence of the Pacific plate indicate that this flow-sustained thermally buoyant temperature gradient extends west ~4000 km from the EPR, across the EPR-superswell system to at least 90 Ma old seafloor. Analysis of the Nazca plate (Figure 9b) is consistent with a continuation of the temperature gradient across the EPR to 102°W, ~1000 km east of the EPR. This scheme, which is illustrated in Figure 11, is in accord with geochemical data [*Woodhead and Devey*, 1993; *Janney et al.*, 2000] which favour a relatively shallow mixing of "normal" depleted mantle and enriched plume material, indicating that vertical flow is not required to be dominant.

[60] The possibility of a lateral sublithospheric pressure-temperature gradient has implications for the origin of large-scale oceanic depth anomalies. Previous models [e.g., *McNutt and Judge*, 1990; *Larson*, 1991; *Larson and Kincaid*, 1996; *McNutt*, 1998; *Sichoix et al.*, 1998] suggest that the Pacific superswell is supported by vertical flow in the asthenosphere. Tomography data limits this to the "diffuse upwelling" of a "pillow" of hot material [*McNutt*, 1998] in the upper mantle which, surviving unreplenished, may be the "near exhausted remnant" of a Cretaceous "superplume" [*Larson*, 1991]. In contrast, the topographic and geophysical observations in the EPR-superswell system favour a general west-to-east horizontal flow. Therefore oceanic depth anomalies are not necessarily the surface expression of vertical motions in the fluid mantle. Rather, the effect of large-scale lateral pressure-temperature variations mediated by horizontal motions may dominate over normal forces on the base of the lithosphere due to changes in vertical flow velocity.

[61] This is not to suggest that there are no focused upwellings in the superswell region. Figure 10 shows, for example, that bathymetry at ~90 Ma is a few hundred m shallower than is the regional, "plate-like" subsidence. The shallowing is localized to the Rarotonga-Society region where it correlates with (Figure 12) a thinned 410–660 km seismic transition zone that indicates a flux at 170°–400°C above ambient temperature [*Niu et al.*, 2002], a free-air gravity anomaly 'high,' and relatively

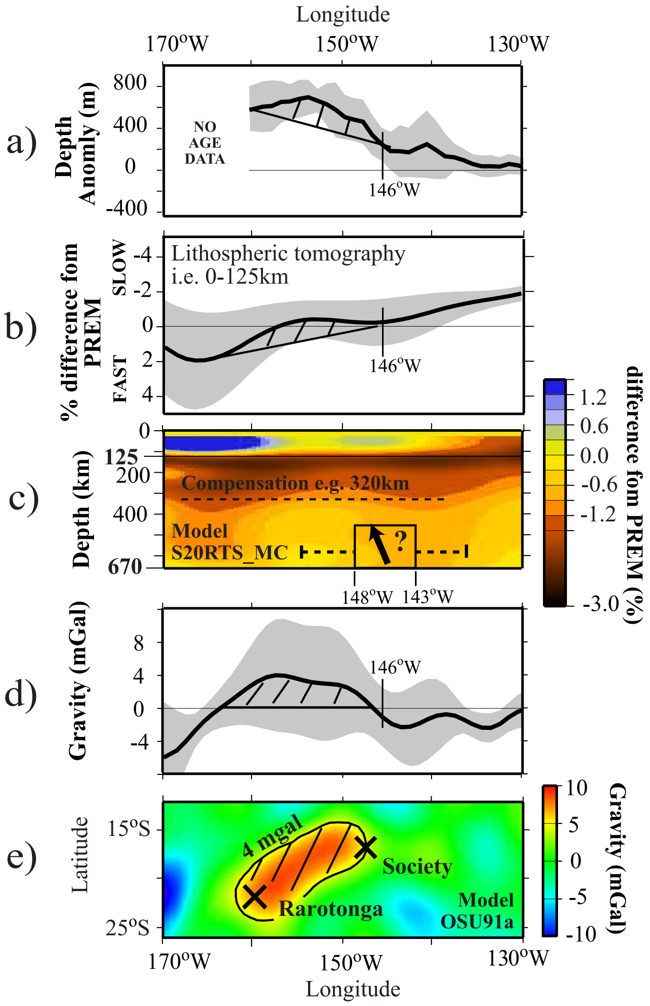

Figure 12. Comparison of depth anomalies to shear wave velocities and gravity anomalies in the Society Islands region. Hachuring indicates anomalies. (a) Depth anomaly in the superswell region. (b) Mean 0–125 km vertical velocity of seismic tomographic model [*Ritsema et al.*, 1999] shown in Figure 12c. The box in Figure 12c is where a locally (radius ~200 km) thinned 410–660 km transition zone indicates upwelling at 170°–400°C above ambient. The arrow schematically illustrates this flux. (d) Profile of the gravity anomaly complete to degree and order 13 to 40 (i.e., $\lambda \simeq 3000-1000$ km) [*Rapp and Pavlis*, 1990] shown in Figure 12e, a gravity anomaly map showing a local high. Note the correlation between the depth anomaly high, seismic velocity low, and gravity anomaly high in the Society Islands region. Bold lines are average (1° mean) with longitude, and grey shading is ±2σ about these means.

slow seismic velocities in the lithosphere [see also *McNutt and Judge*, 1990]. We postulate that this focused influx may cause the large-scale pressure-temperature variations in the region and thus be the ultimate cause of the large-scale depth anomalies.

7.4. Geoid Constraints

[62] One observable that has the potential to constrain our model for large-scale bathymetry, and which we have not discussed yet, is the geoid anomaly. Previous studies, for example, have revealed short-to-intermediate wavelength gravity [*Haxby and Weissel*, 1986] and geoid anomalies [*Cazenave et al.*, 1992] in the EPR-superswell region which have been interpreted, at least in part, in terms of small-scale convection in the sublithospheric mantle that is aligned in the direction of absolute Pacific plate motion. The problem at large scales is that there is disagreement on the sign of the long-wavelength gravitational field over the superswell. After correcting for the cooling lithosphere, *Hager* [1984] and *Watts et al.* [1985], for example, suggest there is a long-wavelength geoid high over the superswell of spherical harmonic degree and order, n, of 2–10 and >10 respectively. On the other hand *McNutt and Judge* [1990] ($n > 4$) and *McNutt* [1998] ($7 < n < 12$) find a geoid low, especially if a thinner, hotter cooling plate than the "standard" [*Parsons and Sclater*, 1977] is used [*McNutt and Judge*, 1990].

[63] The problem therefore relates to which long-wavelength gravitational field best represents the EPR-superswell, system. Our bathymetric observations suggest spatial variations in physical properties within the system of ~4000 km, or ~5000 km if it continues onto the Nazca plate (see Figure 9), corresponding to wavelengths of 8000 ($n = 5$) or 10,000 km ($n = 4$) respectively. Like a cooling lithospheric plate [e.g., *Turcotte and Schubert*, 2002, equation 5–158] this variation can cause long-wavelength geoid effects, so a significant spectral overlap may exist between anomalies associated with the EPR-superswell system and those normally attributed to dynamics in the lower mantle.

[64] Further complications arise from the fact that the geoid increases in spectral power with decrease in n. Therefore geoid wavebands are strongly dependant on the choice of the lowest n. For example, at 154°W (longitude of maximum large-scale shallowing in Figure 9) between 12° and 26°S geoid anomalies for $3 < n < 20$, $4 < n < 20$, $5 < n < 20$, $6 < n < 20$, and $7 < n < 20$ of OUS91a [*Rapp and Pavlis*, 1990] are −18, −6, −9, −14, and −1 m (to the nearest m) respectively. Most of these values become positive after a correction [*Turcotte and Schubert*, 2002, equation 5–158] of +16 m for a "standard" [*Parsons and Sclater*, 1977] plate is applied. To prevent the lowest order dominating and generating artefacts the coefficients should therefore be tapered [*Sandwell and Renkin*, 1988; *Cazenave et al.*, 1992]. Given the probable spectral overlap however, the taper would have to be chosen with care.

[65] A negative geoid anomaly over the superswell would, if present, require factors other than lateral pressure and temperature gradients to be incorporated in a model of the type proposed. A shallowing of the seafloor that is compensated at depth cannot generate a negative gravity anomaly [*McNutt and Judge*, 1990; *McNutt*, 1998], suggesting that an additional mass deficiency is required that does not have a surface expression. One possibility is a component of vertical flow that transmits force incompletely across a low-viscosity layer [see *McNutt*, 1998], perhaps both upward and downward, in a manner suggested by the upper mantle seismic velocity structure (Figure 9b).

[66] Future studies to quantify the relationship between the regional bathymetry as deduced by MiMIC with the long-wavelength geoid anomaly and other observables offer

Table A1. Parameters Used in the Computation of "Up-Warp" ($\mathcal{U}$)[a]

Up-Warp Parameters	Symbol	Value
In-box smoothing width	F_s	0.25
Roughness multiplier	$\mathcal{U}_m$	0.5
Roughness addition	$\mathcal{U}_a$	0.0
Significance cutoff	C_o	0.1

[a] Normally fixed; see Appendix A.

the most promise, we believe, of addressing this problem in the future.

8. Conclusions

[67] We draw the following conclusions from this analysis of bathymetry data in the South Pacific ocean.

[68] 1. The algorithm, MiMIC, is an efficient and effective tool to remove "small-scale" features such as oceanic islands and seamounts, and "medium-scale" hot-spot swells and oceanic plateaus from bathymetric data.

[69] 2. MiMIC is an improvement over previous computer-based techniques such as mean, median, and modal filtering since the bathymetry that remains after processing passes beneath rather through features.

[70] 3. The processed bathymetry reveals the geometry of large-scale, regional, features of the seafloor such as those associated with the superswell and the EPR.

[71] 4. The region of the superswell is associated with a peak shallowing of 712 ± 66 m at 98 Ma, not 1300 m at ~70 Ma as reported by previous workers.

[72] 5. The superswell is part of a larger, continuous, and monotonic depth-age subsidence trend that extends all the way to the EPR crest, not an isolated shallowing that interrupts the ridge-generated subsidence of 40–80 Ma old Pacific oceanic crust.

[73] 6. The monotonic increase in depth anomaly between the EPR and the superswell suggests a single, causative, mechanism acting along the entirety of the trend and thus an "EPR-superswell system."

[74] 7. The monotonic increase can be explained by a model in which the subsidence is caused in part by thermal cooling of a standard [*Parsons and Sclater*, 1977] mid-ocean ridge, and in part by the buoyancy effects of lateral temperature variations in the sub-lithospheric mantle. The best fit model is one in which the temperature above 320 km increases from ~1323°C beneath the EPR to ~1391°C beneath the superswell.

[75] 8. The lateral temperature gradient deduced above is consistent with the observations of the MELT experiment at the EPR if it is accompanied by an across-axis flow. Thus we propose that lateral flow is prevalent throughout the EPR-superswell area and sustains the lateral temperature gradient.

Appendix A: Computational Details of the MiMIC Algorithm

[76] This appendix contains further computational details of the MiMIC algorithm, in particular the up-warp test from the morphological assessment. Specifically, the form of the reasonable upwarp $\mathcal{U}(x)$, the computational definition of the significant bathymetric highs and lows to which this upwarp is compared, and details of that comparison. The morphological assessment is conducted upon a "high," namely a relatively shallow section of bathymetric profile, found by the search construct. Each high is between (x_i, z_i) and (x_s, z_s) along the profile, and distances and heights considered in the assessment are normalized (see main text).

A1. Form of $\mathcal{U}(x)$

[77] Up-warp as a function of distance along profile, $\mathcal{U}(x)$, is defined for x_{frac} in the range $0 < x_{frac} < 1$ (i.e., $x_i < x < x_s$), and is more fully written as $\mathcal{U}(x_{frac})$. Empirically, we find that the maximum visually reasonable up-warp in the center of the box $\mathcal{U}_{\max}$ is linearly related to the roughness of the bathymetry $\mathcal{R}$ by

$$\mathcal{U}_{\max} = \mathcal{U}_m \cdot \mathcal{R} + \mathcal{U}_a \qquad \text{(A1)}$$

where $\mathcal{U}_m$ and $\mathcal{U}_a$ are constants, empirically found to be most usefully set at 0.5 and 0.0 respectively (Table A1). Here, $\mathcal{R}$ is the median absolute deviation (MAD) of the first differences of normalized heights smoothed (sliding arithmetic mean) using a box-car with a width a fraction (F_s) of the section's width. F_s = 0.25 (Table A1). First differences $\left(\frac{\Delta z}{\Delta x}\right)$ are the gradient between consecutive data points, i.e., $\frac{z_{n+1}-z_n}{x_{n+1}-x_n}$. MAD's are the robust [*Box*, 1953] equivalent of standard deviation, where MAD = $median\left|\frac{\Delta z}{\Delta x} - centre\right|$ with *centre* being $median\left(\frac{\Delta z}{\Delta x}\right)$. Stability of this roughness estimator to outliers is important, and MAD's are widely used [e.g., *Rousseeuw and Croux*, 1993; *Swallow and Kianifard*, 1996; *Crowley*, 1997; *Zarow*, 1997; *O'Neal et al.*, 2000], and rigorously determined [*Hogel et al.*, 1994; *Falk*, 1997; *David*, 1998], to provide this robustness. With the normalization and smoothing $\mathcal{R}$ appears independent of scale, section aspect ratio (height:length), and the spatial density of measured data.

[78] Here, although other forms could by used, the gradient $\left(\frac{d\mathcal{U}(x)}{dx}\right)$ of $\mathcal{U}(x)$ changes linearly across the section (i.e., $\frac{d^2\mathcal{U}(x)}{dx^2} = constant$) from $+\alpha$ at x_0 (i.e., $x_{frac} = 0$) to $-\alpha$ at x_1. Integrating under the these conditions (i.e., at x_0, $\frac{d\mathcal{U}}{dx} = \tan \alpha$ and $\mathcal{U} = 0$, at x_s, $\frac{d\mathcal{U}}{dx} = -\tan \alpha$ and $\mathcal{U} = 0$) gives

$$\mathcal{U}(x) = x \tan \alpha (1 - x) \qquad \text{(A2)}$$

The maximum up-warp in the center of the box is

$$\mathcal{U}_{\max} = \mathcal{U}_{x=\frac{1}{2}} = \frac{1}{4} \tan \alpha \qquad \text{(A3)}$$

So, getting $\tan\alpha$ in terms of $\mathcal{U}_{\mathrm{m}}$ and $\mathcal{R}$ by eliminating $\mathcal{U}_{\max}$ from equation (A1) and (A3), substituting values for $\mathcal{U}_a$ and $\mathcal{U}_m$, then substituting into equation (A2) gives

$$\mathcal{U}(x) = 2\mathcal{R}x(1 - x) \qquad \text{(A4)}$$

A2. Visually Significant Points: Definition and Computation

[79] Within a bathymetric section delimited by the "search construct," significant points in the bathymetry are the maxima and minima at the top and bottom of visually significant peaks and valleys respectively. The

visual significance or impact of points as both maxima and minima relates to their location and topographic surroundings. For all x_n we quantify visual significance through horizontal and vertical ranges of dominance.

[80] As a minimum, for example, a point x_n is dominant over a symmetrical range (i.e., centered on x_n) within which it is the lowest point. This range of dominance is calculated by considering points incrementally further away (in both directions) from x_n until a point deeper than z_n is encountered. For example, as a low, a point that has no lower points within 0.2 (normalized units) either side of it has a horizontal significance (Δ_H) of 0.4. If the limits of the box surrounding the section are reached (i.e., $n = i$ or $n = s$) this also limits the range. Similar is done for each point as a maximum.

[81] Vertical significance (Δ_V) may now be deduced. For a low, Δ_V is the mean height difference between it and the two most horizontally dominant peaks to either side of it within its range (as a minima) of horizontal dominance. Thus a low at a height of 0.1 units, neighbored by peaks of heights 0.4 and 0.6 units, would have a $\Delta_V = 0.4$. A similar procedure is used for peaks. The overall significance Δ_{TOT} is then $\Delta_H \times \Delta_V$, and points with a $\Delta_{TOT} \geq$ a cut-off value, C_o, of 0.1 (Table A1), can be said to be significant. The normalization of distances and heights permits C_o to have a single value. In addition, significant peaks must be separated by a low, and visa versa, so it is sometimes necessary to upgrade an intermediate point to "significant" status. Also, both ends of the section and the highest point within the section are arbitrarily given significances of 1.

A3. Success or Failure of the Up-Warp Test

[82] To conduct the up-warp test the linear baseline between (x_i, z_i) and (x_s, z_s) is up-warped to its maximum reasonable extent (equation (A4)). This up-warped baseline is then compared to the significant points in the bathymetry by evaluating $z_{baseline-upwarp}$ (depth, z, and up-warp are positive) for each significant x_n from $n = i$ to $n = s$. If any $z_n \geq z_{baseline-upwarp}$ this implies that a baseline may be reasonably drawn through the valley bottom, namely the section is better described as ≥ 2 sub-sections. The section therefore fails the morphological assessment. Comparison if done with all (i.e., not just significant) x_n commonly produces false failures, for example at the ends of the section.

[83] **Acknowledgments.** We thank Paul Wyer, Steve Usher, Simon Lamb, and Katie Johnston for their help and comments. We are grateful to Frederik Simons, Marcia MuNutt, and an anonymous reviewer for their useful and constructive comments. The production of many of the figures was assisted by the GMT software [*Wessel and Smith*, 1998]. This work was supported by a NERC Studentship to J.H. and a NERC/ROPA award to A.B.W.

References

Bartoszewicz, A. (2000), Chattering attenuation in sliding mode control systems, *Control Cybernetics*, *29*, 585–594.

Bemis, K. G., and D. K. Smith (1993), Production of small volcanoes in the superswell region of the South Pacific, *Earth Planet. Sci. Lett.*, *118*, 251–262.

Binard, N., R. Hekinian, J. L. Cheminee, et al. (1991), Morphology and structural studies of the Society and Austral hotspot regions in the South Pacific, *Tectonophysics*, *186*, 293–312.

Binard, N., R. Hekinian, and P. Stoffers (1992), Morphological study and type of volcanism of submarine volcanoes over the Pitcairn hot-spot in the South Pacific, *Tectonophysics*, *206*, 245–264.

Bonneville, A., V. Clouard, P. Beuzart, I. Klaucke, R. L. Sauve, B. Loubrieu, P. Saget, and Y. Thomas (1997), Possible control of Society Islands volcanism by a preexisting volcanic chain, *Eos Trans. AGU*, *78*(46), Fall Meet. Suppl., Abstract T52B-02.

Box, G. E. P. (1953), Non-normality and tests on variances, *Biometrika*, *40*, 318–335.

Boyd, F. R., and R. H. McCallister (1976), Densities of sterile and fertile garnet peridotites, *Geophys. Res. Lett.*, *3*, 509–512.

Buck, R., and E. M. Parmentier (1986), Convection beneath young oceanic lithosphere: Implications for thermal structure and gravity, *J. Geophys. Res.*, *91*, 1961–1974.

Calmant, S. (1987), The elastic thickness of the lithosphere in the Pacific Ocean, *Earth Planet. Sci. Lett.*, *85*, 277–288.

Calmant, S., and A. Cazenave (1987), Anomalous elastic thickness of the oceanic lithosphere in the south central Pacific, *Nature*, *328*, 236–238.

Canales, J. P., R. S. Detrick, S. Bazin, A. J. Harling, and J. A. Orcutt (1998), Off-axis crustal thickness across and along the East Pacific Rise within the MELT area, *Science*, *280*, 1218–1221.

Caress, D. W., M. K. McNutt, R. S. Detrick, and J. C. Mutter (1995), Seismic imaging of hotspot-related underplating beneath the Marquesas Islands, *Nature*, *373*, 600–603.

Carslaw, H. S., and J. C. Jaeger (1959), *Conduction of Heat in Solids*, 63 pp., Oxford Univ. Press, New York.

Cazenave, A., S. Houry, B. Lago, and K. Dominh (1992), Geosat-derived geoid anomalies at medium wavelength, *J. Geophys. Res.*, *97*, 7081–7096.

Clouard, V., and A. Bonneville (2001), How many Pacific hot-spots are fed by deep-mantle plumes?, *Geology*, *29*, 695–698.

Cochran, J. R. (1986), Variations in subsidence rates along intermediate and fast spreading mid-ocean ridges, *J. Geophys. Res.*, *87*, 421–454.

Conder, J. A., D. W. Forsyth, and E. M. Parmentier (2002), Asthenospheric flow and assymetry of the East Pacific Rise MELT area, *J. Geophys. Res.*, *107*(B12), 2344, doi:10.1029/2001JB000807.

Creager, K. C., and T. H. Jordan (1986), Slab penetration into the lower mantle beneath the Mariana and other island arcs of the northwest Pacific, *J. Geophys. Res.*, *91*, 3573–3589.

Crough, S. T. (1978), Thermal origin of mid-plate hot-spot swells, *Geophys. J. R. Astron. Soc.*, *55*, 451–469.

Crowley, L. G. (1997), Robust statistical estimators for use within competatitve bid data, *J. Construct. Eng. Manage.*, *123*, 53–63.

David, H. A. (1998), Early sample measures of variability, *Stat. Sci.*, *13*, 368–377.

Detrick, R. S., and S. T. Crough (1978), Island subsidence, hot-spots and lithospheric thinning, *J. Geophys. Res.*, *83*, 1236–1244.

Dietz, R. S., and H. W. Menard (1953), Hawaiian swell, deep, and arch, and subsidence of the Hawaiian islands, *J. Geol.*, *61*, 99–113.

Evans, R. L., et al. (1999), Asymmetric electrical structure in the mantle beneath the East Pacific Rise at 17°S, *Science*, *286*, 752–756.

Falk, M. (1997), On MAD and comedians, *Ann. Inst. Stat. Math.*, *49*, 615–644.

Filmer, P. E., M. K. McNutt, and C. J. Wolfe (1993), Elastic thickness of the lithosphere in the Marquesas and Society islands, *J. Geophys. Res.*, *98*, 19,565–19,577.

Filmer, P. E., M. K. McNutt, H. F. Webb, and D. J. Dixon (1994), Volcanism and archipelagic aprons in the Marquesas and Hawaiian islands, *Mar. Geophys. Res.*, *16*, 385–406.

Fleitout, L., and C. Moriceau (1992), Short-wavelength geoid, bathymetry and the convective pattern beneatht the Pacific Ocean, *Geophys. J. Int.*, *110*, 6–28.

Forsyth, D. W., S. C. Webb, L. M. Dorman, and Y. Shen (1998a), Phase velocities of Rayleigh waves in the MELT experiment on the East Pacific Rise, *Science*, *280*, 1235–1238.

Forsyth, D. W., et al. (1998b), Imaging the deep seismic structure beneath a mid-ocean ridge: The MELT experiment, *Science*, *280*, 1215–1218.

Fowler, C. M. R. (1990), *The Solid Earth*, Cambridge Univ. Press, New York.

Goodwillie, A. M. (1995), Short-wavelength gravity lineations and unusual flexure results at the Puka volcanic ridge system, *Earth Planet. Sci. Lett.*, *136*, 297–314.

Goodwillie, A. M., and A. B. Watts (1993), An altimetric and bathymetric study of elastic thickness in the Central Pacific ocean, *Earth Planet. Sci. Lett.*, *118*, 311–326.

Grevemeyer, I., W. Weigel, and C. Jennrich (1998), Structure and ageing of oceanic crust at 14°S on the East Pacific Rise, *Geophys. J. Int.*, *135*, 573–584.

Hager, B. H. (1984), Subducted slabs and the geoid: Constraints on mantle rheology and flow, *J. Geophys. Res.*, *89*, 6003–6015.

Hager, B., and R. Clayton (1989), Constraints on the structure of mantle convection using seismic observations, flow models, and the geoid, in *Mantle Convection*, edited by W. R. Peltier, pp. 657–763, Gordon and Breach, Newark, N. J.

Haxby, W. F., and J. K. Weissel (1986), Evidence for small-scale mantle convection from Seasat altimeter data, *J. Geophys. Res.*, *91*, 3507–3517.

Hogel, J., W. Schmid, and W. Gaus (1994), Robustness of the standard-deviation and other measures of dispersion, *Biometr. J.*, *36*, 411–427.

Ito, G., M. McNutt, and R. L. Gibson (1995), Crustal structure of the Tuamotu Plateau, 15°S, and implications for its origin, *J. Geophys. Res.*, *100*, 8097–8114.

Janney, P. E., J. D. Macdougall, J. H. Natland, and M. A. Lynch (2000), Geochemical evidence from the Pukapuka ridge system for a shallow enriched mantle domain beneath the South Pacific superswell, *Earth Planet. Sci. Lett.*, *181*, 47–60.

Jordahl, K. A., M. K. McNutt, H. F. Webb, S. E. Kruse, and M. G. Kuyendall (1995), Why are there no earthquakes on the Marquesas Fracture Zone?, *J. Geophys. Res.*, *100*, 24,431–24,447.

Jordan, T. H. (1979), Mineralogies, densities and seismic velocities of garnet lherzolites and their geophysical implications, in *The Mantle Sample: Inclusions in Kimberlites and Other Volcanics*, edited by F. R. Boyd and H. O. A. Meyer, pp. 1–14, AGU, Washington, D. C.

Jordan, T. H., H. W. Menard, and D. K. Smith (1983), Density and size distribution of seamounts in the eastern Pacific inferred from wide-beam sounding data, *J. Geophys. Res.*, *88*, 10,508–10,518.

Larson, R. L. (1991), Latest pulse of Earth—Evidence for a midcretaceous superplume, *Geology*, *19*, 547–550.

Larson, R. L., and C. Kincaid (1996), Onset of mid-cretaceous volcanism by elevation of the 670 km thermal boundary layer, *Geology*, *24*, 551–554.

Levitt, D. A., and D. T. Sandwell (1996), Modal depth anomalies from multibeam bathymetry: Is there a South Pacific superswell?, *Earth Planet. Sci. Lett.*, *139*, 1–16.

Lin, R. S., and Y. C. Hsueh (2000), Multichannel filtering by gradient information, *Signal Process.*, *80*, 279–293.

Manglik, A., and U. R. Christensen (1997), Effect of mantle depletion buoyancy on plume flow and melting beneath a stationary plate, *J. Geophys. Res.*, *102*, 5019–5028.

Marty, J. C., and A. Cazenave (1989), Regional variations in subsidence rate of oceanic plates: A global analysis, *Earth Planet. Sci. Lett.*, *94*, 301–315.

McAdoo, D. C., and D. T. Sandwell (1989), On the source of cross-grain lineations in the central Pacific gravity field, *J. Geophys. Res.*, *94*, 9341–9352.

McKenzie, D. (1984), The generation and compaction of partially molten rock, *J. Petrol.*, *25*, 713–763.

McKenzie, D., and M. Bickle (1988), The volume of melt generated by extension of the lithosphere, *J. Petrol.*, *29*, 625–679.

McNutt, M. (1998), Superswells, *Rev. Geophys.*, *36*, 211–244.

McNutt, M., and A. Bonneville (2000), A shallow chemical origin for the Marquesas swell, *Geochem. Geophys. Geosys.*, *1* doi:10.1029/1999GC000028.

McNutt, M. K., and K. M. Fischer (1987), The South Pacific superswell, in *Seamounts, Islands and Atolls*, *Geophys. Monogr. Ser.*, vol. 43, edited by B. H. Keating et al., pp. 25–34, AGU, Washington D. C.

McNutt, M., and A. V. Judge (1990), The superswell and mantle dynamics beneath the South Pacific, *Science*, *248*, 969–975.

McNutt, M., and L. Sichoix (1996), Modal depths from shipboard bathymetry: There IS a South Pacific superswell, *Geophys. Res. Lett.*, *23*, 3397–4000.

McNutt, M. K., D. W. Caress, J. Reynolds, K. A. Jordahl, and R. A. Duncan (1997), Failure of plume theory to explain midplate volcanism in the southern Austral islands, *Nature*, *389*, 479–482.

Menard, H. W. (1973), Depth anomalies and the bobbing motion of drifting islands, *J. Geophys. Res.*, *78*, 5128–5137.

Menard, H. W., and M. McNutt (1982), Evidence for and consequences of thermal rejuvenation, *J. Geophys. Res.*, *87*, 8570–8580.

Montagner, J. P., and T. Tanimoto (1991), Global upper mantle tomography of seismic velocities and anisotropies, *J. Geophys. Res.*, *96*, 20,337–20,351.

Morgan, J. P., and W. H. F. Smith (1992), Flattening of the seafloor depth-age curve as a response to asthenospheric flow, *Nature*, *359*, 524–527.

Morgan, W. (1971), Convection plumes in the lower mantle, *Nature*, *230*, 42–43.

Müller, R. D., and W. R. Roest (1997), Digital isochrons of the world's ocean floor, *J. Geophys. Res.*, *102*, 3211–3214.

National Oceanic and Atmospheric Administration (NOAA) (1988), Digital relief of the surface of the Earth, *Data Announce. 88-MGG-02*, Natl. Geophys. Data Cent., Boulder, Colo.

National Oceanic and Atmospheric Administration (NOAA) (2003a), GEODAS version 4.1, http://www.ngdc.noaa.gov/mgg/gdas/g4_sys.Html, Natl. Geophys. Data Cent., Boulder, Colo.

National Oceanic and Atmospheric Administration (NOAA) (2003b), 5-minute total sediment thickness grid, http://www.ngdc.noaa.gov/mgg/sedthick/sedthick.html, Natl. Geophys. Data Cent., Boulder, Colo.

Niu, F., S. C. Solomon, P. G. Silver, D. Suetsugu, and H. Inoue (2002), Mantle transition-zone structure beneath the South Pacific superswell and evidence for a mantle plume underlying the Society hot-spot, *Earth Planet. Sci. Lett.*, *198*, 371–380.

O'Hara, M. J. (1975), Is there an Icelandic mantle plume?, *Nature*, *253*, 708–710.

O'Neal, M. R., J. R. Frankenberger, D. R. Ess, and R. H. Grant (2000), Precipitation variability at the farm scale during crop phenological phases, *Trans. ASAE*, *43*, 1449–1458.

Oxburgh, E. R., and E. M. Parmentier (1977), Compositional and density stratification in oceanic lithosphere—Causes and consequences, *J. Geol. Soc. London*, *133*, 343–355.

Parsons, B., and J. Sclater (1977), An analysis of the variation of ocean floor bathymetry and heat flow with age, *J. Geophys. Res.*, *82*, 803–827.

Patriat, M., F. Klingelhoefer, D. Aslanian, I. Contrucci, M.-A. Gutscher, J. Talandier, F. Avedik, J. Francheteau, and W. Weigel (2002), Deep crustal structure of the Tuamotu Plateau and Tahiti (French Polynesia) based on seismic refraction data, *Geophys. Res. Lett.*, *29*(14), 1656, doi:10.1029/2001GL013913.

Phipps-Morgan, J., W. J. Morgan, and E. Price (1995), Hotspot melting generates both hotspot volcanism and a hotspot swell, *J. Geophys. Res.*, *100*, 8045–8062.

Rapp, R. H., and N. K. Pavlis (1990), The development and analysis of geopotential coefficient models to spherical harmonic degree-360, *J. Geophys. Res.*, *95*, 21,885–21,911.

Renkin, M. L., and J. G. Sclater (1988), Depth and age in the North Pacific, *J. Geophys. Res.*, *93*, 2919–2935.

Ribe, N. M., and U. R. Christensen (1999), The dynamical origin of Hawaiian volcanism, *Earth Planet. Sci. Lett.*, *171*, 517–531.

Ritsema, J., H. J. van Heijst, and J. H. Woodhouse (1999), Complex shear wave velocity structure imaged beneath Africa and Iceland, *Science*, *286*, 1925–1928.

Robinson, E. M. (1988), The topographic and gravitational expression of density anomalies due to melt extraction in the uppermost oceanic mantle, *Earth Planet. Sci. Lett.*, *90*, 221–228.

Rousseeuw, P. J., and C. Croux (1993), Alternatives to the median absolute deviation, *J. Am. Stat. Assoc.*, *88*, 1273–1283.

Sandwell, D. T., and M. Renkin (1988), Compensation of swells plateaus in the North Pacific: No direct evidence for mantle convection, *J. Geophys. Res.*, *93*, 2775–2783.

Scheirer, D., and D. W. Forsyth (1998), Shipboard geophysical indications of assymetry and melt production beneath the East Pacific Rise near the MELT experiment, *Science*, *280*, 1221–1224.

Schroeder, W. (1984), The empirical age-depth relation and depth anomalies in the Pacific Ocean, *J. Geophys. Res.*, *89*, 9873–9883.

Sclater, J. G., L. A. Lawver, and B. Parsons (1975), Comparison of long-wavelength residual elevation and free air gravity anomalies in the North Atlantic and possible implications for the thickness of the lithospheric plate, *J. Geophys. Res.*, *80*, 1031–1042.

Sichoix, L., A. Bonneville, and M. K. McNutt (1998), The seafloor swells and superswell in French Polynesia, *J. Geophys. Res.*, *103*, 27,123–27,133.

Simons, F. J., M. T. Zuber, and J. Korenaga (2000), Isostatic response of the Australian lithosphere: Estimation of the effective elastic thickness and anisotropy using multitaper spectral analysis, *J. Geophys. Res.*, *105*, 19,163–19,184.

Smith, D. K. (1988), Shape analysis of Pacific seamounts, *Earth Planet. Sci. Lett.*, *90*, 457–466.

Smith, D. K. (1996), Comparison of the shapes and sizes of seafloor volcanoes on Earth and "pancake" domes on Venus, *J. Volcanol. Geotherm. Res.*, *73*, 47–64.

Smith, D. K., and T. H. Jordan (1988), Seamount statistics in the Pacific ocean, *J. Geophys. Res.*, *93*, 2899–2918.

Smith, W. H. F. (1990), Marine geophysical studies of seamounts in the pacific ocean basin, Ph.D. thesis, Columbia Univ., New York.

Smith, W. (1993), On the accuracy of digital bathymetric data, *J. Geophys. Res.*, *98*, 9591–9603.

Smith, W. H. F., and D. T. Sandwell (1994), Bathymetric prediction from dense satellite altimetry and sparse shipboard bathymetry, *J. Geophys. Res.*, *99*, 21,803–21,824.

Smith, W. H. F., and D. T. Sandwell (1997), Global sea floor topography from satellite altimetry and ship depth soundings, *Science*, *277*, 1956–1962.

Smith, W. H. F., and P. Wessel (1990), Gridding with continuous curvature splines in tension, *Geophysics*, *55*, 293–305.

Stein, C. A., and D. H. Abbott (1991), Heat flow constraints on the South Pacific superswell, *J. Geophys. Res.*, *96*, 16,083–16,099.

Stein, C. A., and S. Stein (1992), A model for the global variations in oceanic depth and heat flow with lithospheric age, *Nature*, *359*, 123–129.

Swallow, W. H., and F. Kianifard (1996), Using robust scale estimators in detecting multiple outliers in linear regression, *Boimetrics*, *52*, 545–556.

Talandier, J., and E. A. Okal (1987), Crustal structure in the Society and Tuamotu islands, *Geophys. J. R. Astron. Soc.*, *88*, 499–528.

Thomson, D. J., and A. D. Chave (1991), Jackknifed error estimates for spectra, coherences, and transfer functions, in *Advances in Spectrum Analysis and Array Processing*, *Adv. Ref. Ser.*, chap. 2, pp. 58–113, Prentice-Hall, Old Tappan, N. J.

Toomey, D. R., W. S. D. Wilcock, S. C. Solomon, W. C. Hammond, and J. A. Orcutt (1998), Mantle seismic structure beneath the MELT region of the East Pacific Rise from P and S wave tomography, *Science*, *280*, 1224–1227.

Turcotte, D. L., and G. Schubert (2002), *Geodynamics*, 2nd ed., Campridge Univ. Press, New York.

Van Wykhouse, R. (1973), Synbaps, *Tech. Rep. TR-233*, Natl. Oceanogr. Off., Washington, D. C.

Watts, A. B., D. P. McKenzie, B. E. Parsons, and M. Roufosse (1985), The relationship between gravity and bathymetry in the Pacific Ocean, *Geophys. J. R. Astron. Soc.*, *83*, 263–298.

Webb, S. C., and D. W. Forsyth (1998), Structure of the upper mantle under the EPR from waveform inversion of regional events, *Science*, *280*, 1227–1229.

Wessel, P. (1998), An empirical method for optimal robust regional-residual separation of geophysical data, *Math. Geol.*, *30*, 391–408.

Wessel, P., and W. H. F. Smith (1998), New, improved version of Generic Mapping Tools released, *Eos Trans. AGU*, *79*, 579. [version 3.1]

Wessel, P., L. W. Kroneke, and D. Bercovici (1996), Pacific plate motion and undulations in the geoid and bathymetry, *Earth Planet. Sci. Lett.*, *140*, 53–66.

White, R. S., D. McKenzie, and R. K. O'Nions (1992), Oceanic crustal thickness from seismic measurements and rare-earth-element inversions, *J. Geophys. Res.*, *97*, 19,683–19,715.

Winterer, E. L., and D. T. Sandwell (1987), Evidence from en-echelon cross-grain ridges for tensional cracks in the Pacific plate, *Nature*, *329*, 534–537.

Wolfe, C. J., and S. C. Solomon (1998), Shear wave splitting and implications for mantle flow beneath the MELT region of the East Pacific Rise, *Science*, *280*, 1230–1232.

Wolfe, C. J., M. K. McNutt, and R. S. Detrick (1994), The Marquesas archipelagic apron—Seismic stratigraphy and implications for volcano growth, mass-wasting and crustal underplating, *J. Geophys. Res.*, *99*, 13,591–13,608.

Woodhead, J. D., and C. W. Devey (1993), Geochemistry of the Pitcairn seamounts: Source character and temporal trends, *Earth Planet. Sci. Lett.*, *116*, 81–99.

Xia, Y., X. H. Yu, and W. Oghanna (2000), Adaptive robust fast control for induction motors, *IEEE Trans. Indust. Electr.*, *47*, 854–862.

Yanada, H., and H. Ohnishi (1999), Frequency-shaped sliding mode control of an electrohydraulic servo-motor, *J. Syst. Control Eng.*, *213*, 441–448.

Yatawara, N., B. Abraham, and J. F. MacGregor (1991), A Kalman filter in the presence of outliers, *Commun. Stat. Theory Methods*, *20*, 1803–1820.

Zarow, R. (1997), Adult height prediction in boys by various methods, *Biol. Sport*, *14*, 193–198.

J. K. Hillier and A. B. Watts, Department of Earth Sciences, University of Oxford, Parks Road, Oxford OX1 3PR, UK. (johnh@earth.ox.ac.uk; tony@earth.ox.ac.uk)